Superconducting prepolarization coil for ultra-low-field MRI

Iiro Lehto

School of Science

Thesis submitted for examination for the degree of Master of Science in Technology.

Espoo 27.11.2017

Thesis supervisor:

Prof. Risto Ilmoniemi

Thesis advisor:

Koos Zevenhoven, M.Sc.

Aalto University
School of Science

AALTO UNIVERSITY
SCHOOL OF SCIENCE

ABSTRACT OF THE
MASTER'S THESIS

Author: Iiro Lehto

Title: Superconducting prepolarization coil for ultra-low-field MRI

Date: 27.11.2017 Language: English Number of pages: 6+49

Department of Neuroscience and Biomedical Engineering

Professorship: Biomedical Engineering

Supervisor: Prof. Risto Ilmoniemi

Advisor: Koos Zevenhoven, M.Sc.

Magnetic resonance imaging (MRI) allows the structure of matter to be studied by measuring magnetic signals emitted by proton spins in response to applied magnetic fields. Ultra-low-field (ULF) MRI at microtesla-range fields is an emerging technology with promising clinical applications, particularly in brain imaging. To increase the low magnetization of the imaged sample and the strength of the measured signal, sample polarization in a strong ($\sim 10-100$ mT) magnetic field prior to the ULF-MRI measurements is invariably used in present ULF-MRI instrumentations.

To perform the sample prepolarization, a strong electromagnet that can be quickly ramped is required. This prepolarization electromagnet is typically realized using resistive copper conductors. Such coils, however, are large, effectively exciting unwanted transient eddy currents, require effective cooling, and possibly increase the system noise level due to thermally agitated electrons. Therefore, a compact superconducting magnet, sharing the helium bath with the SQUID sensors, is an attractive, although less used, alternative. Unfortunately, the superconducting magnets also come with their unique challenges. Superconductors are magnetized in external magnetic fields, which is the root of the greatest difficulties, as ULF MRI is sensitive to distortions in the measurement field.

In this thesis, I will discuss the challenges in designing a superconducting prepolarization coil for ULF MRI that produces prepolarization pulses exceeding 100 mT, while minimally distorting other fields after the prepolarization. Methods for achieving these goals are proposed, and a small test coil was constructed to test how simulations compare with experimental measurements. The measurements show that achieving these goals should be possible with a full-sized prepolarization coil.

Keywords: Ultra-low-field magnetic resonance imaging, superconductor, coil, magnetization, vortex

AALTO-YLIOPISTO
PERUSTIETEIDEN KORKEAKOULU

DIPLOMITYÖN
TIIVISTELMÄ

Tekijä: Iiro Lehto

Työn nimi: Suprajohtava esipolarisointikela ultramatalan kentän magneettikuvaukseen

Päivämäärä: 27.11.2017 Kieli: Englanti Sivumäärä: 6+49

Neurotieteen ja lääketieteellisen tekniikan laitos

Professuuri: Lääketieteellinen tekniikka

Työn valvoja: Prof. Risto Ilmoniemi

Työn ohjaaja: DI Koos Zevenhoven

Magneettikuvauksella (MRI) voidaan tutkia aineen rakennetta mittaamalla protonien spinien lähettämää magneettista signaalia ulkoisessa magneettikentässä. Ultramatalan kentän (ULF) MRI mikroteslaluokan kentissä on tekniikka, jolla on lupaavia kliinisiä sovelluskohteita, erityisesti aivokuvantamisen parissa. Tutkittavan näytteen matalan magnetisaation ja heikon signaalin kasvattamiseksi nykyisissä ULF-MRI-laitteissa käytetään poikkeuksetta näytteen polarisointia voimakkaassa ($\sim 10-100$ mT) magneettikentässä ennen itse ULF-MRI-mittauksia.

Esipolaroinnin suorittamiseksi tarvitaan voimakas sähkömagneetti, jonka virtaa pitää pystyä myös muuttamaan nopeasti. Tämä sähkömagneetti on tyypillisesti toteutettu resistiivisillä kuparijohtimilla. Tällainen ratkaisu johtaa suureen kelaan, joka aiheuttaa epätoivottuja pyörrevirtatransientteja, vaatii tehokasta jäähdytystä ja saattaa nostaa laitteen kohinatasoa elektronien lämpöliikkeen seurauksena. Näistä syistä kompakti suprajohtava sähkömagneetti samassa heliumkylvyssä SQUID-sensoreiden kanssa on mielenkiintoinen, joskin vähemmän käytetty, vaihtoehto. Valitettavasti myös suprajohtaviin magneetteihin liittyy omat haasteensa. Suurimmat haasteet pohjautuvat suprajohteiden magnetoitumiseen ulkoisessa kentässä, sillä ULF MRI on herkkä mittauskentän vääristymille.

Tässä työssä käsittelen haasteita liittyen suprajohtavan esipolarisaatiokelan suunnitteluun, jolla päästäisiin yli 100 mT kentänvoimakkuuteen minimaalisilla mittauskentän vääristymillä. Menetelmiä tämän tavoitteen saavuttamiseksi ehdotetaan ja pieni testikela valmistettiin, jotta simulaatioita pystyttiin vertaamaan kokeellisiin havaintoihin. Mittaukset osoittavat, että tavoitteiden saavuttaminen pitäisi olla mahdollista täysikokoisella esipolarisointikelalla.

Avainsanat: Ultramatalan kentän magneettikuvaus, suprajohde, kela, magnetisaatio, vorteksi

Contents

Symbols and abbreviations

Symbols

C	Volumetric heat capacity
$\vec{B}$	Magnetic field
$\vec{B}_0$	Static measurement field
$\vec{B}_1$	Excitation field
$\vec{B}_\mathrm{p}$	Prepolarization field
$\vec{H}$	Magnetic H-field
H_c	Thermodynamic critical field
H_c1	Lower critical field
H_c2	Upper critical field
$\hbar$	Reduced Planck constant
I	Electric current
$\vec{J}$	Current density
$\vec{J}_c$	Critical current density
k	Thermal conductivity
k_B	Boltzmann constant
L	Inductance
$\vec{M}$	Magnetization
$\vec{m}$	Magnetic moment
P	Power per volume
Q	Heat per volume
$\vec{S}$	Spin angular momentum
T	Temperature
T_c	Critical temperature
T_1	Longitudinal relaxation time
T_2	Transverse relaxation time
t	Time
V_m	Magnetic scalar potential
γ	Gyromagnetic ratio
κ	Ginzburg–Landau parameter
Λ	London coefficient
λ_L	London penetration depth
λ_s	Superconducting fraction
μ_0	Vacuum permeability
ρ	Resistivity
ρ	Radial coordinate
τ	Coupling time constant
Φ	Magnetic flux
Φ_0	Magnetic flux quantum
ω_L	Larmor frequency

Operators

$\frac{\mathrm{d}}{\mathrm{d}t}$	Derivative with respect to variable t
$\frac{\partial}{\partial t}$	Partial derivative with respect to variable t
$E(k)$	Complete elliptic integral of the second kind of modulus k
$K(k)$	Complete elliptic integral of the first kind of modulus k
$\delta(x)$	Dirac delta function of argument x
∇A	Gradient of scalar A
$\nabla \times \vec{A}$	Curl of vector $\vec{A}$

Abbreviations

AC	Alternating (current)
BREAKBEN	Breaking the nonuniqueness barrier in electromagnetic neuroimaging
DC	Direct (current)
DynaCAN	Dynamical coupling for additional dimensions
MRI	Magnetic resonance imaging
MSR	Magnetically shielded room
NMR	Nuclear magnetic resonance
OFHC	Oxygen-free high thermal conductivity
RMS	Root mean square
SNR	Signal-to-noise ratio
SQUID	Superconducting quantum interference device
ULF MRI	Ultra-low-field MRI

1 Introduction

Magnetic resonance imaging (MRI) is a widely used method in clinical imaging, discovered in the 1970s. MRI offers safe, noninvasive imaging with good spatial resolution and soft-tissue contrast. It is based on a phenomenon called nuclear magnetic resonance (NMR), in which atomic nuclei rotate, or precess, about an external magnetic field, emitting and absorbing energy at a certain resonant frequency. In MRI, the magnetic signal emitted by hydrogen nuclei is measured in response to different magnetic fields, giving structural information of the imaged sample [1, 2]. In order to increase the signal-to-noise ratio (SNR), traditional MRI is performed in strong magnetic fields, typically on the order of teslas.

However, recently there has been interest in magnetic resonance imaging in ultra-low-fields (ULF MRI), on the order of $10-100$ μT [3, 4]. A typical approach to reaching a sufficient SNR in ULF MRI is to utilize extremely sensitive superconducting quantum interference device (SQUID) sensors for signal detection, and to prepolarize the sample in a strong magnetic field, on the order of $10-100$ mT. Although ULF MRI does not compete with high-field MRI in terms of the SNR, it offers some unique benefits. The low magnetic fields in ULF MRI allow less expensive and more open device instrumentation, as well as silent operation. ULF MRI can also be combined with other sensitive imaging methods, such as magnetoencephalography (MEG) [5]. In low fields, the T_1 relaxation times are more sensitive to the chemical environment, giving enhanced contrast between different tissues [6]. Novel imaging techniques are also possible with ULF MRI, for example, in current-density imaging [7, 8].

Although the technology has been demonstrated, the full potential of ULF MRI has not been realized, and further development in this field is necessary. An ongoing project named BREAKBEN (Breaking the Nonuniqueness Barrier in Electromagnetic Neuroimaging) aims at improving the resolution and reliability of functional human brain imaging. To achieve the goals set in the BREAKBEN project, a new prepolarization coil design is required. During the BREAKBEN project, two MEG–MRI prototype devices are built: an intermediate prototype that allows easier testing of individual components and a final prototype with high performance MEG–MRI functionality for human brain imaging. This work aims to find designs for the prepolarization coils to be used in these prototypes.

In order to reach a good SNR, the prepolarization field should be as high as practical, as the signal strength is proportional to the prepolarization field. A superconducting prepolarization coil has been used in a MEG–MRI device at Aalto University. This has a number of advantages compared to a normal metal coil: the high current density and low losses allow a compact coil to be used in the existing helium bath, and the small amount of resistive metals at low temperature produces only low levels of thermal Johnson–Nyquist noise. The compact size is especially useful in ULF MRI, as such a coil is more easily shielded to induce weaker eddy currents in the MSR walls, which produce secondary fields detrimental to ULF-MRI image quality. If a resistive coil were used, it would have to be built larger to fit outside the helium dewar, making it harder to shield efficiently. In addition, a resistive coil would

require effective cooling to withstand the necessary high currents. Unfortunately, the superconducting coils also come with their unique challenges. Superconductors are magnetized in external field, distorting other applied fields and complicating accurate image reconstruction. Above a certain field, most superconductors allow flux penetration into the bulk of the superconductor in the form of magnetic vortices, and these vortices can remain trapped in the superconductor even after the external field has been removed, leaving the superconductor magnetized. Depending on the choice of the superconductor, also the material-specific critical fields may limit the attainable polarization field strength. And although superconductors are capable of lossless current transport, there are significant loss mechanisms in changing magnetic fields that need to be considered to reach the fast slew rates required. In this work, I will address these issues and propose a coil design for producing a strong prepolarization field with low distortion effects.

In Sec. 2, I will discuss the physical background of ULF MRI and superconductors, focusing on topics relevant to this work. In Sec. 3, the requirements for the prepolarization are analyzed, and a proposed design approach is described. In Sec. 4, measurements of a constructed test coil are presented and compared with simulations. Finally, in Sec. 5, the results are discussed and the work concluded.

2 Background

2.1 Ultra-low-field magnetic resonance imaging

In this section, I will describe the basic physical principles behind MR imaging and explain the common approach for performing MRI at ultra-low-fields, followed by a slightly more detailed discussion on the prepolarization pulses. For further information, the basics of MRI are discussed in many textbooks, such as in Refs.[1, 2]. Also for ULF MRI, a good textbook exists by Kraus *et al.* [4].

2.1.1 MRI basic principles

Certain elementary particles and atomic nuclei posses a quantum mechanical property called spin. This property gives the particles spin angular momentum $\vec{S}$, which can have magnitudes $S = \hbar\sqrt{s(s+1)}$, where s is the spin quantum number, which can take values $0, 1/2, 1, 3/2...$, and $\hbar$ is the reduced Planck constant. Particles with integer spin are called bosons, and particles with half-integer spins fermions. In addition to the spin quantum number s, only one of the components of the spin can be defined at once. This component along a chosen axis is given by $S_z = \hbar s_z$, where s_z is the spin projection quantum number. s_z can take the values $-s, -(s-1), ..., (s-1), s$, giving $2s+1$ possible states for a particle with spin s. When no external magnetic fields are applied, these states have the same energy, i.e., they are degenerate. When an external field is applied, this degeneracy breaks down, which is called the Zeeman effect. For MRI studies, the particle of interest is the proton, i.e., the hydrogen nucleus, as it is abundant in soft-tissues and has a nonzero spin $s = 1/2$. The proton spin has the two possible states $s_z = -1/2$ and $s_z = 1/2$, corresponding to directions anti-parallel (higher energy) and parallel (lower energy) to the external field, respectively. The Zeeman splitting between these two states is given by

$$\Delta E = \hbar\gamma B\,, \tag{1}$$

where γ is the gyromagnetic ratio, a characteristic of the particle in question. For protons, the gyromagnetic ratio is $\gamma_p/(2\pi) = 42.58$ MHz/T. In addition to the angular momentum, particles with spin have a magnetic moment

$$\vec{m} = \gamma\vec{S}\,, \tag{2}$$

which is the property that produces the fields measured in NMR studies. However, at room temperature the Zeeman splitting is typically small compared to the thermal energy, and an enormous number of spins is required to produce measurable signals. Therefore, the quantity of interest is the macroscopic magnetization. In equilibrium, the spins are Boltzmann distributed, and the macroscopic magnetization under the approximation $\Delta E \ll k_{\mathrm{B}}T$ becomes

$$\vec{M}_0 = \frac{\gamma^2\hbar^2\rho_{\mathrm{s}}}{4k_{\mathrm{B}}T}\vec{B}\,, \tag{3}$$

where ρ_{s} is spin density, k_{B} is the Boltzmann constant, and T temperature.

When the magnetization is tilted from its equilibrium state, a torque results, leading to precession around the external field. The frequency of this precession is known as the Larmor frequency

$$\omega_{\mathrm{L}} = \frac{\Delta E}{\hbar} = \gamma B \,. \tag{4}$$

This precession continues while different relaxation processes take the magnetization back towards its static equilibrium. The dynamics of the magnetization is often described by the Bloch equation

$$\frac{\mathrm{d}\vec{M}}{\mathrm{d}t} = \gamma \vec{M} \times \vec{B} + \frac{1}{T_1}\left(\vec{M}_0 - \vec{M}_z\right) - \frac{1}{T_2}\vec{M}_{xy} \,, \tag{5}$$

where $\vec{M}_z$ is the component of $\vec{M}$ parallel to the external field, $\vec{M}_{xy}$ the perpendicular component, and T_1 and T_2 are relaxation times. The longitudinal relaxation time T_1 describes the decay of the longitudinal component toward the equilibrium value, while the transverse relaxation time T_2 describes the decay of the perpendicular component toward zero. The physics of spin dynamics dictates that $T_2 < 2\,T_1$, and in most common situations it is observed that $T_2 < T_1$ [9]. The relaxation times depend on the external field, at 1.5 T for example, the relaxation times of cerebrospinal fluid (CSF) are $T_1 = 4.5$ s and $T_2 = 2.2$ s, which are quite large values compared to different human tissues [1].

In MR imaging sequences, the magnetization parallel to the main field $\vec{B}_0$ is first tipped by pulsing an excitation field $\vec{B}_1$ oscillating at the resonant frequency ω_{L}. For the strongest signal, a 90° flip angle should be used. After this, different gradient fields are applied, giving a spatially varying measurement field and Larmor frequencies. This allows spatial information to be encoded into the measured NMR signal. This procedure is typically repeated multiple times, until enough information is gathered for image reconstruction. The measured signal is basically the projection of the magnetization onto different spatial frequencies, and with a suitable encoding strategy, the image can be reconstructed simply by an inverse Fourier transform.

The NMR signal in high-field MRI is measured using receiver coils based on the Faraday induction. The flux Φ through the receiver coil produced by the magnetized sample can be written using the reciprocity principle

$$\Phi(t) = \int_{\mathrm{sample}} \vec{\mathcal{B}}(\vec{r}) \cdot \vec{M}(\vec{r}, t)\, \mathrm{d}^3 r \,, \tag{6}$$

where $\vec{\mathcal{B}}$ is the lead field, produced by unit current in the pickup coil [1]. The voltage induced in the pickup coil is proportional $\mathrm{d}\Phi/\mathrm{d}t$, i.e., proportional to both the magnetization magnitude and the Larmor frequency. Thus, the measured signal strength has a B_0^2 dependence, as the equilibrium magnetization and ω_{L} are both proportional to B_0. This is the reason that has led the development of traditional MRI into higher and higher fields. Today, 3-T fields are used for routine human MRI.

2.1.2 MRI in ultra-low fields

Ultra-low-field MRI (ULF MRI) means MR imaging at field strengths on the order of 10−100 μT [5, 10, 11]. The B_0^2 scaling of signal strength presents a challenge for ULF MRI with a measurement field some five orders of magnitude lower than in traditional MRI. This challenge is typically overcome by measuring the signal with extremely sensitive superconducting quantum interference device (SQUID) sensors and by prepolarizing the sample in a field $\vec{B}_\mathrm{p}$ much stronger than the measurement field $\vec{B}_0$.

The SQUID sensors consist of a superconducting flux transformer coupled to a superconducting quantum interference device. The SQUID is a superconducting loop, interrupted by one (RF SQUID) or two (DC SQUID) Josephson junctions, which are thin layers of insulator material or normal metal. The DC SQUID is the common choice for biomedical applications, and therefore the RF SQUID will not be further discussed in this text. The operation of the SQUID is based on quantum mechanical phenomena. The flux through the SQUID is quantized in units of a flux quantum $\Phi_0 = \pi\hbar/e$, and the maximum supercurrent through the Josephson junctions is a periodic function of the input flux. The Josephson junctions are shunted by a resistance, which produces a voltage whenever the critical current is exceeded. When the SQUID is current biased, the voltage over the SQUID becomes periodic in the input flux. A schematic of a SQUID is shown in Fig. 1. A more detailed discussion of SQUID operation can be found in the SQUID handbook [12]. The readout of a SQUID is typically linearized using a flux-locked loop, in which a feedback coil is used to keep the input flux of the SQUID constant. This readout scheme gives a linear response and can maintain optimal sensitivity across the operating range. The flux transformer consists of a pickup coil, which is designed to give a desired sensitivity in the imaging volume, and an input coil, which couples the signal to the SQUID. Typical configurations include magnetometers measuring the magnetic field, and gradiometers measuring different spatial derivatives of the magnetic field. These sensors are extremely sensitive down to DC fields, which makes them suitable for ULF-MRI and MEG applications. The Aalto MEG–MRI device is currently fitted with custom SQUID sensors, designed to tolerate the strong $\vec{B}_\mathrm{p}$ pulses [13]. These sensors have a noise level of about 5 fT/$\sqrt{\mathrm{Hz}}$. During the BREAKBEN project, VTT Technical Research Centre of Finland Ltd. is developing next generation SQUID sensors, aiming at noise levels below 0.5 fT/$\sqrt{\mathrm{Hz}}$ and 10−20 ms recovery times after 150−200 mT pulses.

To reduce noise from outside sources, the ULF-MRI coil system and sensors are typically located inside a magnetically shielded room (MSR). The MSR is layered with highly conductive metal sheets, possibly together with highly permeable μ-metal sheets. Aluminum is a typical choice for the conducting layers due to its low weight and good mechanical properties. Eddy currents in the conductive layers provide effective shielding against oscillating magnetic fields [14]. The conductive sheets may be welded together carefully to allow the eddy currents to form freely. ULF-MRI measurements can be successfully performed with only conductive shielding and coils canceling the earth's static magnetic field, provided that the Larmor frequencies

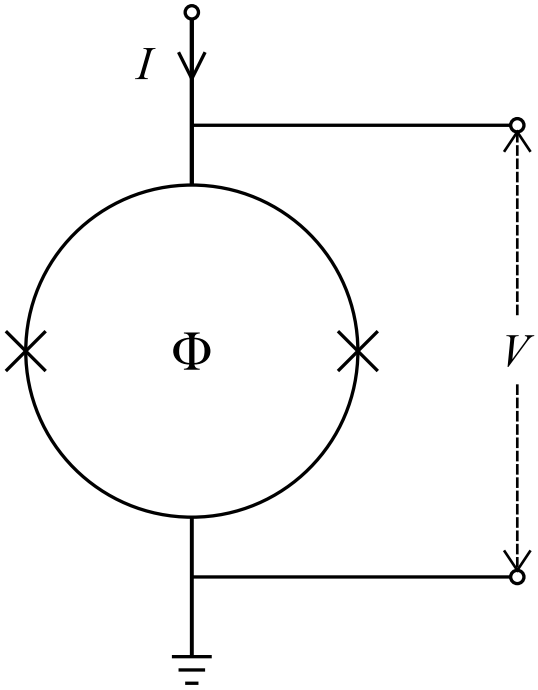

Figure 1: A SQUID with bias current I, output voltage V, and input flux Φ. The crosses denote the Josephson junctions.

used are sufficiently high [14]. The μ-metal layers are effective in shielding low-frequency fields, and therefore necessary for MEG measurements, where weak signals at frequencies as low as 1 Hz are measured [15]. The Aalto MEG–MRI sensor array and coil setup is located inside a magnetically shielded room with two layers of aluminum and μ-metal sheets, manufactured by Euroshield Ltd.

The combination of a magnetically shielded room and strong pulsed fields introduces a problem with induced eddy currents in the conductive MSR walls. After the prepolarization and other preparatory pulses, there can be significant transient secondary fields from the induced eddy currents in the MSR walls, distorting spin dynamics and delaying the start of signal acquisition. To reduce the induced eddy currents, the prepolarization coil stray field can be reduced by using a self-shielded coil. Nieminen *et al.* [16] have designed shielding coils that cancel the lowest-order multipole moments of a main coil. Another method to reduce the eddy currents is to use DynaCAN waveforms fed to a separate coil, designed to drive the eddy currents to zero after the prepolarization pulse [17].

The strength of the prepolarization field should be chosen as strong as practical. Besides the technical difficulties with the $\vec{B}_\mathrm{p}$ electromagnet itself, the most important limiting factors are the field tolerance of SQUID sensors and the induced eddy currents in the MSR walls. The prepolarization pulses and electromagnets are further discussed in the following section.

2.1.3 Prepolarization

The prepolarization of spins in ULF MRI is achieved by pulsing a strong electromagnet. Field strengths on the order of 10−100 mT have been used [3, 5, 10, 11], the higher fields producing a stronger magnetization and signal. The $\vec{B}_\mathrm{p}$ field is first ramped up, then held constant for a period of time comparable to T_1 to produce the spin polarization, and finally ramped down. The ramp-down can be performed either adiabatically or non-adiabatically. Non-adiabatic ramp-down means fast ramps where the field rotates with a much higher angular frequency ψ than that of the Larmor precession ($\psi \gg \omega_\mathrm{L}$). Assuming the polarization pulse has been long enough, such a fast ramp leaves the magnetization in the equilibrium state dictated by $\vec{B}_\mathrm{p}$, according to Eq. (3). The precession around $\vec{B}_0$ will begin immediately after the ramp-down.

An adiabatic ramp-down means ramps where the field rotation is much slower than the Larmor precession ($\psi \ll \omega_\mathrm{L}$). Taking, for example, a linear ramp-down with orthogonal $\vec{B}_0$ and $\vec{B}_\mathrm{p}$, this condition becomes [4]

$$\left|\frac{\mathrm{d}B_\mathrm{p}}{\mathrm{d}t}\right| \ll \gamma B_0^2 \,. \tag{7}$$

Assuming field strengths $B_0 = 100$ μT, $B_\mathrm{p} = 100$ mT and $\psi = \omega_\mathrm{L}/100 = \omega_\mathrm{L}/\alpha$, the length of the linear ramp-down becomes an unreasonable 4 s. However, choosing a ramp-down profile optimal for fast adiabatic ramp-downs, the time required becomes [4]

$$T_\mathrm{off} = \frac{\alpha}{\gamma B_0} \int_0^{B_\mathrm{p}/B_0} \frac{\mathrm{d}\xi}{(1+\xi)\sqrt{1+\xi^2}} \,. \tag{8}$$

Using the same parameters, such a ramp-down can be accomplished in only 5 ms.

During an adiabatic ramp the magnetization is able to track the rotation of the field, and after the ramp the magnetization is aligned with $\vec{B}_0$. Hence, after an adiabatic ramp, an excitation pulse is required to introduce spin precession. A non-adiabatic ramp-down allows the NMR signal to be generated sooner after the prepolarization, resulting in less spin relaxation and a stronger signal. However, this benefit can be offset by other transient effects after the $\vec{B}_\mathrm{p}$ pulse, such as SQUID sensor recovery and secondary field effects from eddy currents, delaying the start of the signal acquisition. A benefit of adiabatic ramp-down is that the direction of the magnetization is set by the $\vec{B}_0$ field, which is typically more homogeneous than $\vec{B}_\mathrm{p}$. Therefore, the inhomogeneity of $\vec{B}_\mathrm{p}$ affects only the magnetization magnitude, and the resulting variation in image brightness is easily corrected after reconstruction. With longer ramp-downs, also the coupling losses in filamentary superconductors can be reduced, as further discussed in Sec. 2.3.3. By shaping the ramp-down profile, it is also possible to achieve, for example, some defluxing of superconducting parts.

Producing these relatively short and strong pulses introduces some technical challenges. Resistive prepolarization coils require effective cooling, which has been achieved using either liquid nitrogen or water cooling [3, 11]. Thick normal conductors also carry thermal currents, producing fields detrimental for ULF-MRI image quality. The field coupled to the SQUID sensors from the Nyquist–Johnson noise current

is proportional to the wire diameter squared, which has led to the use of stranded litz conductors, which, on the other hand, are more difficult to cool efficiently [18]. Building a resistive coil outside the liquid helium dewar results in a fairly large coil. Effectively shielding such a coil and dealing with the secondary fields from the induced currents in the MSR walls can be difficult compared with a more compact coil realized inside the dewar.

The approach presently used in the Aalto MEG–MRI device is to use a superconducting prepolarization magnet sharing the helium bath with the SQUID sensor array [5]. The high current density and low losses of superconducting wire allow compact coils to be realized inside the liquid helium dewar. The small amount of normal metals at low temperature also produces very little magnetic noise due to Nyquist–Johnson noise currents. However, the choice of a superconducting coil also comes with its unique challenges. Superconducting materials are magnetized in external fields, distorting the imaging fields and affecting spin dynamics. The maximum field obtainable can be limited by the critical fields of the superconductor, depending on the choice of materials. There are also loss mechanisms in superconducting wires, especially with quickly pulsed fields, that need to be considered to maintain the operating temperature of the superconductor and to limit helium boil-off.

The present prepolarization coil in the Aalto MEG–MRI device consists of three parts: a main superconducting coil with one superconducting and one normal copper shielding coil. This reduces the stray field by 90 % at 1-m distance on the coil axis [5]. The superconducting parts are made of multifilament niobium conductor. This coil can achieve fields up to 60 mT, and remanent magnetization is observed after pulses exceeding 22 mT. For the BREAKBEN project, a goal has been set to exceed 100 mT without remanent field issues.

2.2 Superconductivity

Superconductivity is a phenomenon in which a material loses its electrical resistivity at low temperatures. This happens as electrons pair up as bosons and assume a lower energy state. These so-called Cooper pairs are not scattered by the surrounding lattice, allowing lossless transport of electric current. Due to their unique properties, superconductors are favored over normal conductors in many applications, although the operation requires costly cooling systems.

Superconductivity can be accurately modeled using the thermodynamic Ginzburg–Landau theory, or the microscopic Bardeen–Cooper–Schrieffer theory. In this thesis, however, we will use a simple macroscopic quantum model, as it is easier to comprehend and can explain the relevant phenomena. In this section, I will introduce the basic superconductor phenomena and models relevant to this work. For a more thorough discussion on the physics of superconductivity, the reader is referred to the textbooks [19, 20].

2.2.1 Basic properties and type-I superconductors

The superconducting state only exist under the right conditions. Superconductivity can be destroyed by increasing temperature T, external field H, or current density J. A superconductor phase diagram for a niobium–titanium alloy is shown in Fig. 2. The diagram shows the critical surface, below which superconductivity always prevails and above which the material behaves as a normal conductor. The critical temperature T_c is the temperature at which the critical current density J_c and critical field become zero. For typical niobium–titanium alloys, the critical temperature is around 9.8 K, depending on the composition [21]. In zero magnetic field, the transition between the normal and the superconducting state is a second-order transition, meaning there is no latent heat [20].

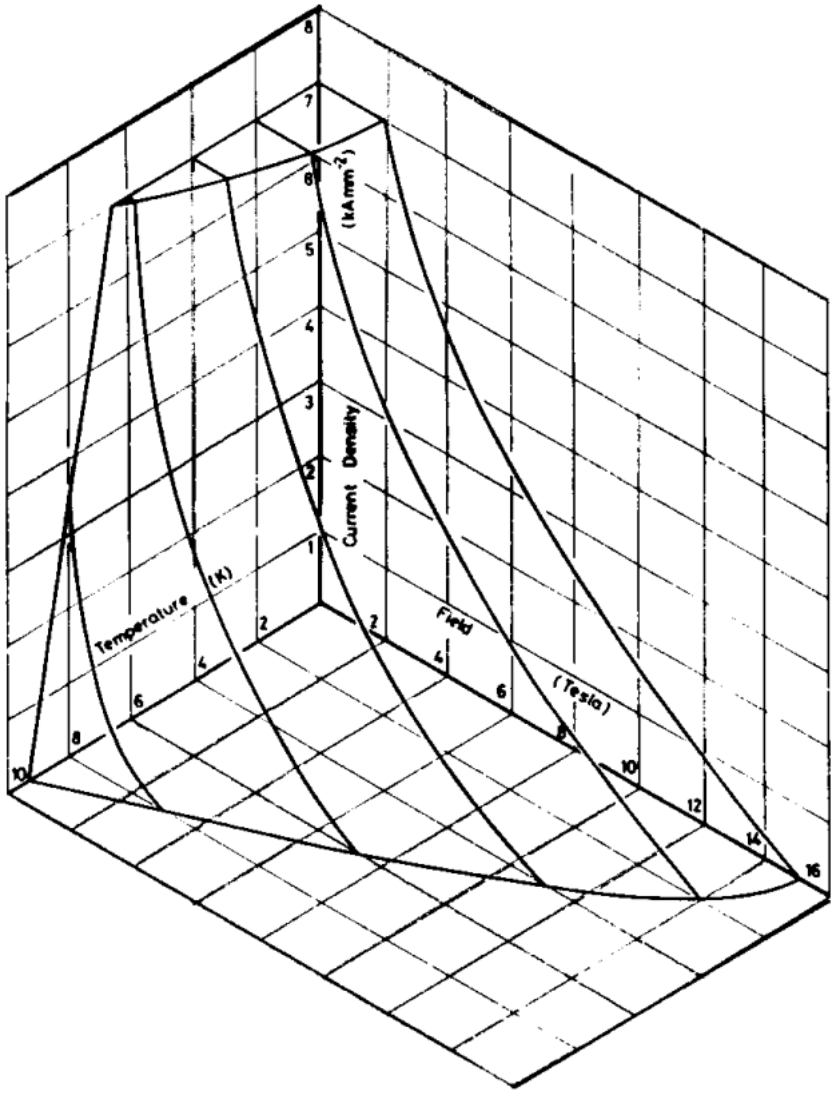

Figure 2: A superconductor phase diagram showing the critical surface. Figure from Ref. [22].

Infinite conductivity is a fundamental property of superconductivity. The relation between the electric field $\vec{E}$ and the supercurrent density $\vec{J}$ is given by the first London equation

$$\vec{E} = \frac{\partial}{\partial t}\left(\Lambda \vec{J}\right) . \tag{9}$$

Λ is the London coefficient, given by $\Lambda = m_\mathrm{e}/(2\rho_\mathrm{C} e^2)$, where m_e is the electron mass, e elementary charge, and ρ_C is the density of Cooper pairs. Here we can interpret that the only force impeding the motion of the Cooper pairs is the inertial force. Thus, the motion of the Cooper pairs is not impeded by scattering, as with normal electrons, allowing lossless transport of current.

Perfect conductivity is not the only implication of superconductivity. Another fundamental property of superconductors is the Meissner effect, in which external fields are always expelled from the interior of the superconductor, i.e., superconductors behave as perfect diamagnets. The infinite conductivity and Lenz's law alone imply that the magnetic field inside a superconductor cannot change. However, when superconductors are cooled down from a temperature above T_c in an external field, field expulsion is again observed, which is the unique property of the Meissner effect. Combining the first London equation (9) with the Faraday's law $\nabla \times \vec{E} = -\partial \vec{B}/\partial t$, we get

$$\nabla \times \frac{\partial}{\partial t}\left(\Lambda \vec{J}\right) = -\frac{\partial \vec{B}}{\partial t} . \tag{10}$$

When this equation is integrated with respect to time, the Meissner effect dictates that the constant of integration has to be zero. This gives us a constitutional equation for superconductors, the second London equation

$$\nabla \times \left(\Lambda \vec{J}\right) = -\vec{B} . \tag{11}$$

Combining this with Ampere's law $\nabla \times \vec{B} = \mu_0 \vec{J}$, we find

$$\nabla^2 \vec{B} = \frac{\mu_0}{\Lambda}\vec{B} , \tag{12}$$

where we can read off a characteristic length $\lambda_\mathrm{L} = \sqrt{\Lambda/\mu_0}$, called the London penetration depth. This gives the depth to which external field can penetrate in a superconductor, as it is exponentially attenuated. The penetration depths for typical superconductors are quite small, for example, for niobium $\lambda_\mathrm{L} = 85$ nm [19]. Therefore, for many type-I superconductors, the shielding currents can be thought of as surface currents.

Flux quantization is another implication of superconductivity. The Cooper pairs in a superconductor all condense into the same ground state, allowing them to be described by a macroscopic wavefunction

$$\Psi(\vec{r}) = \sqrt{\rho_q\left(\vec{r}\right)} \exp\left(i\theta\left(\vec{r}\right)\right) , \tag{13}$$

where $\rho_q(\vec{r})$ is the charge density and $\theta(\vec{r})$ the phase of the complex wavefunction. Using the Schrödinger equation, one can derive an equation for the macroscopic current density

$$\Lambda \vec{J} = \frac{\hbar}{2e}\nabla\theta - \vec{A} , \tag{14}$$

where $\vec{A}$ is the magnetic vector potential [19]. Integrating this expression along a closed path C enclosing a surface S gives

$$\oint_C \Lambda \vec{J} \cdot \mathrm{d}\vec{l} + \int_S \vec{B} \cdot \mathrm{d}\hat{s} = \frac{\hbar}{2e} \oint_C \nabla\theta \cdot \mathrm{d}\vec{l}, \tag{15}$$

where Stokes's theorem has been used to transform the integral involving $\vec{A}$. The integral over the gradient of the phase is simply the change in phase when traversing the integration path. The wave function has to be single-valued at all points, limiting this phase change to a multiple of 2π. This gives the flux quantization condition

$$\oint_C \Lambda \vec{J} \cdot \mathrm{d}\vec{l} + \int_S \vec{B} \cdot \mathrm{d}\hat{s} = n\Phi_o \,, \tag{16}$$

where n can take the values $0, \pm1, \pm2, \pm3, ...$ and $\Phi_0 = \pi\hbar/e$ is the flux quantum. For simply connected superconducting regions the integrations paths can be shrunk infinitesimally small, which guarantees $n = 0$ in such cases. Inserting $n = 0$ into Eq. (16) actually recovers the second London equation (11), which can be expected as this is the constitutive relation in simply connected regions. However, in multiply connected regions n can take nonzero values. Keeping the integration path inside the superconductor, well away from the boundaries, guarantees the current density to be vanishingly small. In such cases, the flux Φ quantization condition (16) becomes

$$\Phi = n\Phi_0 \,. \tag{17}$$

This can be evidenced by cooling a superconducting loop in an external field. The flux trapped inside the loop is always a multiple of the flux quantum, with n chosen such that it matches the flux before the transition as closely as possible [19].

Type-I superconductors are characterized by the thermodynamic critical field H_c, which gives the condensation energy of the superconducting phase per unit volume as $\frac{1}{2}\mu_0 H_\mathrm{c}^2$. This means that H_c is the field at which the condensation energy equals the energy required to push the external field out of the superconductor, and above H_c the superconducting phase is no longer energetically favorable. H_c is also the maximum surface current density a type-I superconductor can carry, as can be seen from the magnetic field interface condition

$$\hat{n} \times \left(\vec{H}_2 - \vec{H}_1\right) = \vec{K} \,, \tag{18}$$

where $\hat{n}$ is the normal of the interface, $\vec{H}_1$ and $\vec{H}_2$ the fields on either side of the interface, and $\vec{K}$ the surface current density. Therefore, for a cylindrical conductor with radius a in the absense of external fields, $2\pi a H_\mathrm{c}$ is the maximum transport current. This limits the usefulness of type-I superconductors in electrical wires, as only the surface can contribute to current transport. Using filamentary wires, the current transport capability can be increased, but the limitation of fairly low critical field in type-I conductors remains. For example, lead (Pb), the only type-I superconductor that has $T_c = 7.20$ K well above the helium boiling point 4.2 K, has a critical field of only $\mu_0 H_c = 80.3$ mT [20]. Therefore, for superconducting wires,

an another class of superconductors is favored, namely type-II superconductors, the subject of the following section.

So far, we have only considered fields in a bulk superconductor, neglecting the effect of the superconductor's shape. These calculations hold, for example, in a superconducting slab with external field parallel to the surfaces, as the field on the surface of the superconductor equals the external field. However, for different geometries, the flux penetration may take place well before the external field reaches the critical field H_c. For example, a long cylinder in the Meissner state placed into a homogeneous transverse external field B_ext focuses the magnetic field near its surface, and the maximum field on the surface becomes $2B_\mathrm{ext}$. Therefore, flux penetration begins in external fields exceeding $H_\mathrm{c}/2$, and the type-I cylinder enters a so-called intermediate state in the range $H_\mathrm{c}/2 < H_\mathrm{ext} < H_\mathrm{c}$, where normal and superconducting regions coexist [20].

2.2.2 Type-II superconductors

Only type-I superconductors show a perfect Meissner effect, as described in Sec. 2.2.1. Type-II superconductors can allow flux to penetrate while retaining infinite conductivity. Below the lower critical field H_c1, type-II conductors behave as type-I conductors, showing the Meissner effect, and above the upper critical field H_c2, superconductivity is destroyed. In the regime $H_\mathrm{c1} < H < H_\mathrm{c2}$, type II superconductors enter the mixed (or vortex) state, in which flux is allowed to penetrate into the bulk of the superconductor in the form of magnetic vortices. These vortices, always enclosing a single flux quantum Φ_0, were first predicted by Abrikosov [23]. If the density of vortices is n_v, the average magnetic field inside the superconductor becomes

$$\langle B \rangle = n_\mathrm{v} \Phi_0 \,. \tag{19}$$

Allowing flux to penetrate is energetically favorable and therefore type-II conductors can remain superconducting in very high fields. For example, niobium–tin (Nb_3Sn) has an upper critical field of $\mu_0 H_\mathrm{c2} = 28$ T [20], allowing very strong magnets to be produced. The magnetization behavior of type-I and type-II superconductors is illustrated in Fig. 3.

The vortices consist of a supercurrent circulating around a tiny normal core. The supercurrent circulating this normal core grows weaker with distance from the core, in accordance with the flux quantization condition (16), the characteristic length being λ_L. Approaching the core of the vortex, the current density increases until it reaches the maximum value possible without breaking the Cooper pairs, the depairing current density $\vec{J}_\mathrm{pair}$. At the depairing current density, the kinetic energy of the Cooper pairs equals their binding energy. This defines the radius of the normal core, giving another length scale characterizing type-II superconductors, the coherence length ξ. For a typical type-II conductor niobium–titanium, these lengths are $\lambda_\mathrm{L} = 300$ nm and $\xi = 4$ nm [19]. The ratio between the penetration depth and the coherence length $\kappa = \lambda_\mathrm{L}/\xi$, known as the Ginzburg–Landau parameter, separates between type-I and type-II superconductors. Superconductors with $\kappa < 1/\sqrt{2}$ have type-I behavior, and those with $\kappa > 1/\sqrt{2}$ behave as type-II [19]. In fact, the transition

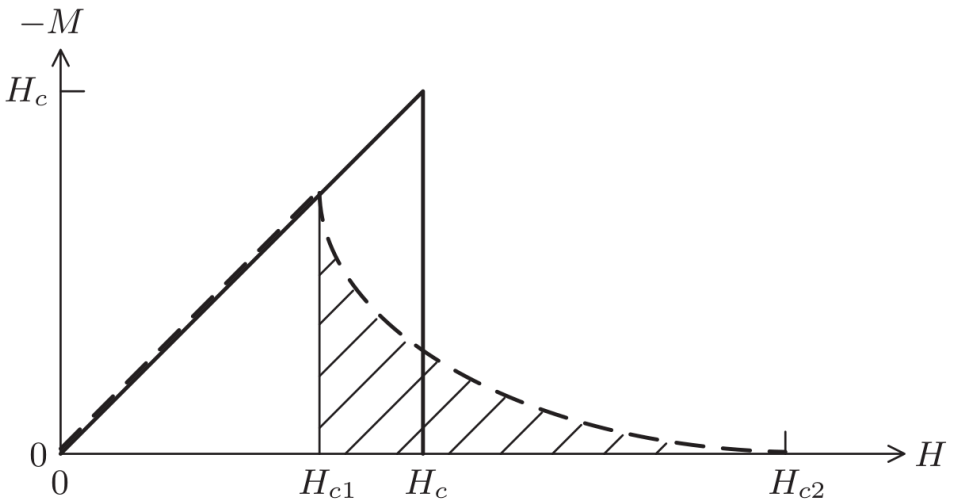

Figure 3: The critical fields and magnetization behavior of type-I (solid line) and type-II (dashed line) superconductors. The hatched region denotes the mixed state for type-II superconductors. Figure adapted from Ref. [21].

between the normal core and the surrounding superconductor is gradual, and the Ginzburg–Landau theory is required for accurate vortex modeling and finding the critical value $\kappa = 1/\sqrt{2}$. However, the simplified model with a normal core is sufficient for understanding the basic vortex interactions.

If a force is applied to a vortex, it will move inside the superconductor. When an external supercurrent $\vec{J}_{\text{ext}}$ flows around a vortex, the vortex feels a Lorentz-like force

$$\vec{F} = \vec{J}_{\text{ext}} \times \Phi_0 \hat{e}_x \,, \tag{20}$$

where $\hat{e}_x$ is the direction of the vortex [19]. When two vortices are placed nearby in a superconductor, the current distributions around the vortices will overlap, leading to an interaction between the vortices. Like vortices repel each other, while vortices with opposite directions are attracted to each other. Due to these forces, opposing vortices will meet and annihilate, while like vortices are arranged into a hexagonal vortex lattice, assuming the vortices are free to move within the superconductor.

H_{c1} is the field at which the vortices become energetically favorable in the superconductor. One of the highest values of H_{c1} in known superconductors is in pure niobium. Reported critical fields for high purity niobium are $\mu_0 H_{\text{c1}} = 140$ mT and $\mu_0 H_{\text{c2}} = 280$ mT [24, 25]. Again, the geometry of the superconductor affects the external field required for flux penetration, allowing vortex nucleation at external fields below H_{c1}. Taking the long cylinder in a transverse field as an example, the mixed state exists in the range $H_{\text{c1}}/2 < H_{\text{ext}} < H_{\text{c2}}$. In addition to this, there are other mechanisms affecting the onset of flux penetration. Vortices near the surface of a superconductor are attracted to the surface due to the boundary condition of no normal current, which can be thought of as a force between the vortex and an opposing image vortex on the other side of the surface [26]. The length of the vortex and its potential energy varies within the superconductor, depending on the geometry.

This results in a line-tension force, pushing out vortices near the surfaces, and forming a so-called geometrical barrier [27]. These effects result in a surface barrier, which can delay the flux penetration in high-κ superconductors. However, even with strong surface effects, flux penetration cannot be delayed above the thermodynamic critical field H_c.

2.2.3 Pinning and the Bean model

To model the magnetization of strongly pinning superconductors, the Bean model, also known as the critical state model, was proposed in the 1960s [28, 29]. As the field around a nonmagnetized type-II superconductor is increased, vortices start penetrating into the superconductor from the surfaces, and become attracted to pinning centers near the surface. These pinning centers are impurities or other defects in the crystal lattice. If, for example, there is a small normal region in the superconductor, a vortex located at this defect will have a lowered free energy, as the volume of the normal core created in the superconductor is lowered. The current distribution resulting from vortex density gradient has a microscopic structure, but is fairly uniform especially for strongly type-II conductors, with high κ. The resulting gradient in the flux density corresponds to a volume current according to Ampere's law

$$\nabla \times \vec{B} = \mu_0 \vec{J}\,. \tag{21}$$

As this current flows around other vortices, they will experience a force given by Eq. (20). Once this force exceeds the pinning force of the vortices, they will be pushed deeper into the superconductor. This current density that is required to move the vortices is known as the critical current density $\vec{J_c}$ for type-II superconductors. In the Bean model, it is assumed that the magnetic field is continuous at the superconductor surface, i.e., there are no surface currents. This assumption is also valid with strongly type-II superconductors well above their H_{c1}. As the external field is changed, this critical current in the superconductor persists, only chancing in direction when necessary to satisfy the boundary condition. Therefore, the Bean model can be summarized with

$$|\nabla \times \vec{H}| = \begin{cases} 0, & \text{where the field has not penetrated,} \\ J_c, & \text{elsewhere}\,. \end{cases} \tag{22}$$

A direct consequence of the Bean model is that, if a superconductor is cooled in zero field, the current-free state is permanently lost once an external field is applied. Even after this initial flux penetration, the magnetization depends on the magnetization history of the superconductor in a hysteretic manner. A magnetization curve predicted by the Bean model is shown in Fig. 4. The curve displays the initial branch showing almost perfect flux expulsion at low fields, when all current flows near the surfaces. Further increasing the field, the magnetization starts leveling out, eventually reaching the saturated state where the magnetization is at a maximum. The area under this curve is actually proportional to the energy lost when the external field is cycled. Therefore, reducing the magnetization is desirable in many AC applications where the losses can be costly.

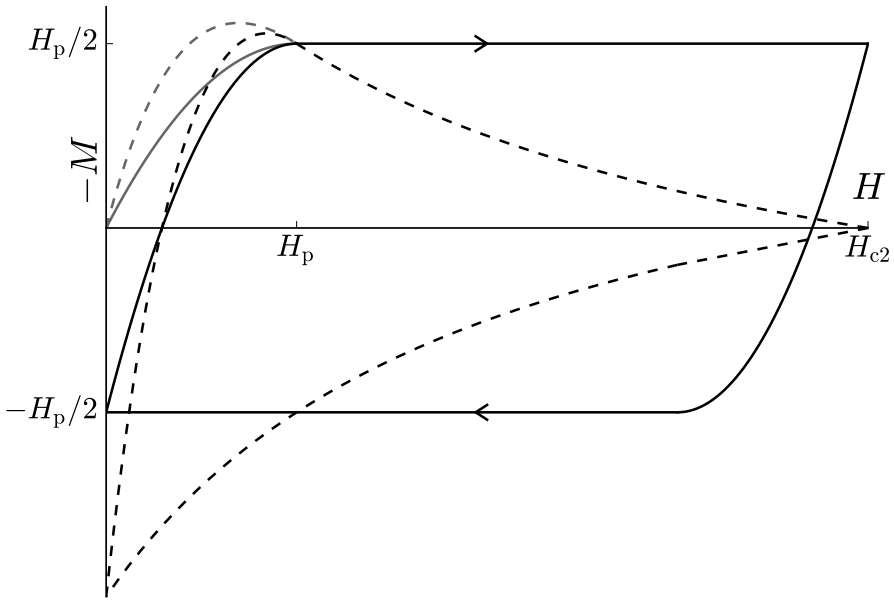

Figure 4: Magnetization in external field, as the field is cycled between 0 and H_{c2}. The solid curve corresponds to the simplified model with constant J_c, and the dashed line to a more realistic $J_c = J_c(H)$ model.

The critical current density is a function of the magnetic field, although in many cases, involving a limited range of fields, $J_c(B, T)$ can be taken as a constant. J_c is related to the vortex-pinning force, affected by factors such as vortex-lattice rigidity and vortex density in relation to pinning-site density. Measurements show that J_c is at a maximum at zero field, and decreases with increasing field, becoming zero at H_{c2}. In measuring J_c at low fields, care must be taken to ensure the measurement does not induce significant fields, as is the case with direct transport current measurements where the transport current will produce a large self-field. Therefore, J_c at low fields is best inferred from magnetization measurements. The zero-field critical current density for Nb–Ti at 4.2 K has been measured to be about $J_c(0\ \mathrm{T}, 4.2\ \mathrm{K}) = 20\ \mathrm{GA/m^2}$ [22, 30].

Exceeding J_c results in vortex motion, which is a dissipative process. This dissipation results in a voltage loss and heating of the superconductor. Therefore, J_c practically also sets the maximum current density the superconductor can carry. This critical current is typically some order of magnitude lower than the depairing current density J_{pair} that can be found near the surface of a type-I superconductor. However, as the interior of a type-II superconductor is also able to carry supercurrents, the maximum transport current in a cylindrical wire of radius a is $\pi a^2 J_c$. For example, niobium–titanium superconductors have $J_c = 2.5\ \mathrm{GA/m^2}$ measured at 5-T external field and 4.2-K temperature [21]. For a 1-mm diameter conductor, this gives a

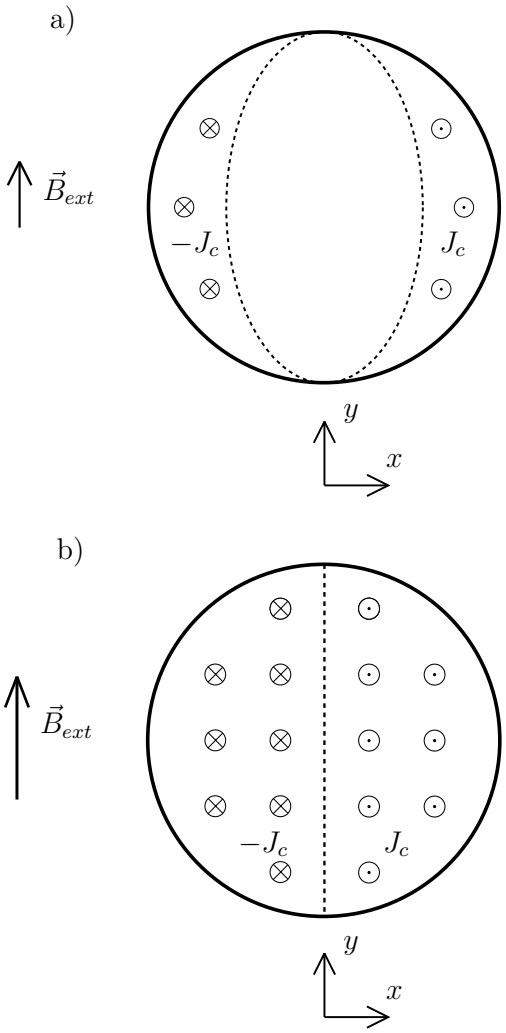

Figure 5: Saturated magnetization in a cylinder with transverse magnetic field.

transport current of 2 kA, which is orders of magnitude larger than would be possible with a similarly sized type-I or normal conductor.

The exact behavior of the magnetization in external field depends on the geometry of the system. For our purposes, a cylindrical filament in a transverse field is the most interesting case. When such a cylinder is cooled in zero field, and the field is ramped up to a low value for the first time, a current density is induced, expelling the magnetic field from the interior of the cylinder. This current flows only near the surfaces, with the critical current density J_c. This situation is shown in Fig. 5a. The magnetic moment m of the cylinder of length l is given by summing over the current loops

$$m = l \int xJ(x,y)\,\mathrm{d}x\mathrm{d}y\,, \tag{23}$$

assuming the coordinate system in Fig. 5. As the field is increased, the shielding current penetrates deeper and deeper into the conductor until the penetration field H_a is reached and current flows in all parts of the conductor. This situation for the saturated state is illustrated in Fig. 5b. The critical current distribution for external fields below H_a requires numerical calculations, as done in Ref. [31] for example. For the saturated case, we know the current distribution from the symmetry of the system, and the magnetic moment of a cylinder of length l can be evaluated from Eq. (23) as

$$m = l \int_{x>0} x J_\mathrm{c} \, \mathrm{d}x\mathrm{d}y - l \int_{x<0} x J_\mathrm{c} \, \mathrm{d}x\mathrm{d}y = 2 l J_\mathrm{c} \int_{x>0} x \, \mathrm{d}x\mathrm{d}y \, . \tag{24}$$

By carrying out the integration, we get

$$m = \frac{4}{3} J_\mathrm{c} l a^3 \, . \tag{25}$$

And dividing by the volume gives the magnetization

$$M = \frac{4}{3\pi} J_\mathrm{c} a \, . \tag{26}$$

In case the average magnetization over a composite conductor is desired, this expression can be multiplied by the superconducting fraction λ_s. This saturated state first occurs at the penetration field H_a, which in the transverse cylinder geometry is given by [32]

$$H_a = \frac{2 a J_\mathrm{c}}{\pi} \, . \tag{27}$$

This gives $\mu_0 H_\mathrm{a} = 16$ mT for a typical Nb–Ti filament with $a = 1$ μm and $J_\mathrm{c} = 20$ GA/m^2. Therefore, for most filamentary conductor applications, penetration takes place at fairly low fields.

Equation (26) reveals that, to lower the saturation magnetization, we should either lower the critical current density or use smaller-diameter wires. Lowering J_c does not help to lower the total magnetic moment, as we would consequently have to use more wires in parallel to achieve the same transport current. Therefore, using conductors made of fine filaments is the common approach to reduce the magnetization. Minimizing the magnetization and losses is important in many applications, and the use of filamentary conductors is extensively discussed in the literature.

The manufacturing processes allow very fine filaments to be produced, but there is a limit as to how far this approach works in lowering the magnetization. The Cooper pairs in a superconducting filament are not tightly bound to the superconducting metal, but are able to penetrate into the surrounding normal metal matrix as well. This process is known as the proximity effect, and it causes fine filaments to appear larger and couple to other nearby filaments, leading to increased magnetization [33, 34, 35]. This magnetization increase scales exponentially with the interfilament distance d_n and external field H, i.e., as $\exp(-d_\mathrm{n}/K_\mathrm{n} - H/H_0)$, where K_n and H_0 are constants [34]. To prevent the proximity coupling in multifilament wires, the

interfilament distance should be kept sufficiently large and a suitable matrix material with low K_n can be chosen to allow a lower d_n. Typical choices for such matrix materials are Cu–Ni and Cu–Mn alloys. In Ref. [35], detectable proximity coupling was measured at $d_\mathrm{n} = 1990$ nm in copper matrix, while an addition of 30 wt.% of nickel reduced this to $d_\mathrm{n} = 110$ nm. Such alloy matrices also have much larger resistivities compared to copper, which affects the stabilizing properties of the matrix, as discussed in the next section, and possibly a composite matrix with pure copper is required.

2.3 Superconducting coils and wires

In this section, I will give a short overview of the phenomena important in superconducting magnet engineering, regarding construction, stability, protection, and losses. For a more detailed discussion of these topics, the reader is referred to Ref. [22].

2.3.1 Mechanical design

Mechanical design is important for superconducting magnets, as there can be strong forces and stresses due to the strong fields. In an ULF-MRI setup, the prepolarization coil is operated in weak external fields; thus there are no significant forces between the different coils. However, there will be strong stresses within the prepolarization coil due to its self-field. As an example, consider a single loop of wire with radius $a = 150$ mm in an axial $B = 2$ T field, carrying a $J = 1$ GT/m^2 current density that produces a tension in the loop. The loop stress σ_θ resulting from the Lorenz force can be calculated as

$$\sigma_\theta = BJa\,. \tag{28}$$

For this example, the loop stress becomes 300 MPa, already exceeding the yield strength of hardened copper $\sigma_\mathrm{Y} = 275$ MPa at 77 K [21]. In a solenoid magnet, the innermost layer will feel the greatest force and the outer layers will feel a weaker opposite force, producing a radial compression in the coil. The forces on a short solenoid coil are visualized in Fig. 6. The radial compression helps share the loop stresses between the different turns, and typical small magnets do not require structural reinforcing. Another possible effect of the Lorenz force are sudden movements of individual turns. When turns held in place by frictional forces break free, the work done on the moving conductor will be released as heat once it is brought back to rest in an impact against another turn. It can be shown that movements on the order of 1 μm can be enough to quench a magnet operating near its critical current [22].

Magnets are typically impregnated with epoxy resin or other materials to support the winding and to stop wire motion. Stresses from the Lorenz force and thermal contraction are likely to cause cracking in the impregnating material, resulting in local heat releases. These heat releases can be large enough to significantly heat a conductor and even quench the magnet. Therefore, fillers are typically added to the impregnating resin to closely match the thermal contraction with the conductors and to better resist large fractures. If a magnet is wound and glued onto a rigid coil former, there can be stresses, fractures, and friction at the winding–coil-former

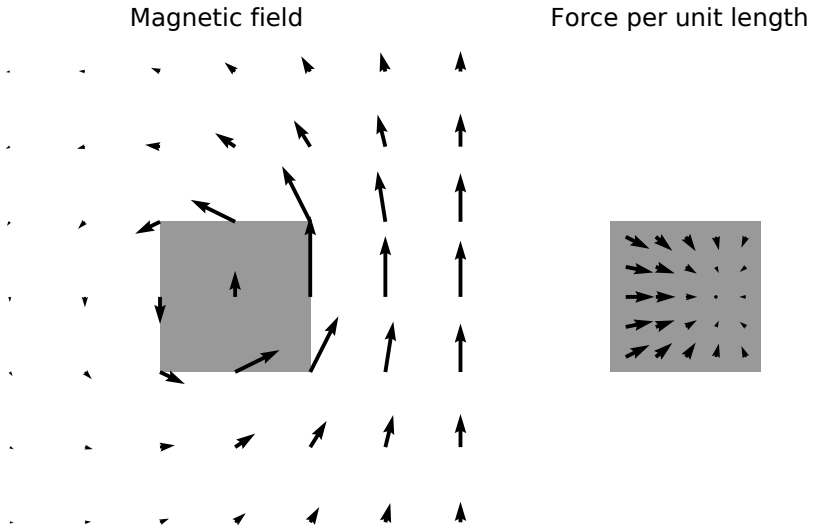

Figure 6: The magnetic field and the Lorenz force per unit length of conductor in a short solenoid coil. The gray areas denote the coil cross-section, which consist of a number of conductors.

interface. To reduce such disturbances, excessively rigid coil-formers with unmatched thermal contraction should be avoided, or the coil formers can be even removed altogether after the winding process [22].

When a new superconducting magnet is operated for the first time, the critical current required for a quench can be quite low, and a few quenches are required before the critical current plateaus at a higher value. This effect is knows as training, and it is observed to be more pronounced in large magnets. It is believed that during training different mechanical changes take place, such as cracking in places where it is inevitable. Once the magnet is trained, there are less disturbances, allowing higher currents to be reached. [22]

2.3.2 Stabilization and protection

In a superconducting magnet, small heat releases will occur due to multiple reasons. These can be point releases, such as those resulting from small movements of the wire or cracking impregnation material, or more distributed, such as those resulting from AC losses of the wire, as discussed in the following section. A conductor transporting exactly its critical current cannot tolerate any heat releases, as this would raise the conductor temperature and lower the critical current density, leading to a temperature runaway. Therefore, superconducting magnets typically cannot reach the critical current measured for a short piece of conductor, which is known as current degradation. To stabilize the conductor against small disturbances, superconducting wires are

typically manufactured with a normal metal matrix, in which superconducting filaments are embedded. Copper has a low normal resistivity and high thermal conductivity, and is therefore typically used in the normal matrix to improve stability.

Flux jumping is another possibly significant source of disturbances. These happen as the shielding current in a type-II superconductor flows with the critical current density $J_c(T)$ as given by the Bean model. $J_c(T)$ is a monotonically decreasing function of temperature; therefore, a small increase in temperature will lower J_c leading to vortex movement. The vortex movement is a dissipative process and further heats the superconductor, again lowering J_c. This cycle may continue, heating the conductor and possibly reaching the normal state. Fortunately, flux jumping is a well understood phenomenon, and can be cured by using sufficiently fine filaments. This requires filament diameter to be below approximately 60 μm for Nb–Ti, and is another reason for the popularity of multi-filament conductors [22].

A small normal zone within a magnet is able to recover via thermal conduction. To appreciate the stabilizing effect of copper, the maximum length of a normal zone that is able to recover, known as the minimum propagation zone, can be calculated. Assuming there is heat conduction only along the axis of the conductor, the length of the minimum propagation zone is proportional to $\sqrt{k/\rho}$, being only about 0.5 μm for a pure Nb–Ti conductor [22]. For pure copper, the factor $\sqrt{k/\rho}$ is some three orders of magnitude larger, explaining the good performance of composite conductors with a copper matrix.

Small normal zones are able to recover solely by the effect of heat conduction. However, when effective cooling is available, larger normal zones can be recovered as well. This is known as cryogenic stabilization. When heat generation in the volume of the conductor is less than the heat transfer through its surface, normal zones can recover. The heat transfer achieved by boiling liquid helium surrounding the coil is strongly dependent on the temperature of the cooled surface, as well as the surface quality or coating of the surface. For thin conductors, the temperature inside the conductors can remain uniform due to heat conduction. However, inside larger conductors or windings the temperature can be significantly higher compared to the surface. Therefore, for large magnets, the addition of cooling channels may be necessary to improve the cryogenic stabilization.

Quenching the magnet during normal use should be avoided by proper use and design of the magnet. However, there is always a possibility of quenching, and therefore magnets should be designed to quench safely. A quench typically begins as a small length of conductor turns normal due to a local disturbance or cooling failure. This normal volume will expand due to heat conduction and ohmic heating, which increases the resistance of the coil and results in a current decay. During a quench, the current drops to zero, while the inductive energy $LI^2/2$ stored in the magnet needs to be dissipated. If this energy was entirely dissipated in the magnet, and evenly distributed over the winding, quenching would not be an issue. However, a large part of this energy is likely dissipated near the point of the quench onset, unless specific protection schemes are used. Excessive local heating will induce thermal stresses, likely damaging the magnet before the conductor would melt or the

insulation would char. A temperature rise under 200 K is typically considered safe [21]. Another aspect that should be considered is the voltage developed across the resistive normal zone, as a large voltage can possibly damage the insulation, even if the temperature rise is within safe limits.

To calculate the maximum temperature at the point of the quench onset, a conservative approximation is to assume an adiabatic process in which heat is not conducted within the conductor or transferred to the helium bath. This is also a realistic approximation, as the heat generation during a quench is much larger compared to normal operation. The heat balance at the point of quench onset can be written

$$J^2(t)\rho(T)\mathrm{d}t = C(T)\,\mathrm{d}T\,, \tag{29}$$

where t is time and C is the volumetric heat capacity. Rearranging and integrating this expression gives [22]

$$\int_0^\infty J^2(t)\,\mathrm{d}t = J_0^2 t_\mathrm{d} = \int_{T_0}^{T_\mathrm{max}} \frac{C(T)}{\rho(T)}\,\mathrm{d}T = U(T)\,. \tag{30}$$

Thus, the relevant material properties with their temperature dependencies can be represented by the single function $U(T)$. Knowing the characteristic time of the current decay t_d, this equation can be used to determine whether the heat increase is within a tolerable bound. For magnets without additional protection schemes, t_d can be estimated by modeling the propagation of the normal zone, which gives the resistance and the current decay in the magnet [22].

Small magnets can be self-protecting, i.e., the current decay in a shorted magnet is fast enough to limit the temperature rise. In case a magnet is not self-protecting, some additional protection scheme should be implemented to decrease t_d and keep the magnet safe. Such protection schemes can be divided into passive and active protection. Passive protection schemes include adding coupled secondary windings and shunting sections of the magnet with resistors or diodes. However, these are not suitable options for AC magnets. Active protection means monitoring the magnet and initiating quench protection measures whenever a quench is detected. These measures include fast discharging of the magnet into a power supply or into an external dump resistor, and heating the coil with additional heater elements to achieve a faster resistance growth. External discharge of the stored energy has the added benefit of saving a large amount of helium during quenches.

Typical DC magnets are low voltage devices, which allows current supplies to be neglected in magnet protection. For AC magnets where powerful current supplies are required, as in ULF-MRI use, it is important to turn off the current supplies soon after a quench to limit the helium boil-off, even if the magnet was self-protecting. This requires monitoring of the magnet to detect quenches. For the Aalto ULF-MRI system, a quench detection system has been implemented that monitors the current and voltage of the magnet and detects when these measurements are incompatible with a model of the superconducting coil.

2.3.3 Losses

Although superconductors allow lossless current transport, there are many losses in practical superconducting wires and coils, especially when operated with AC currents. These losses are small when compared with normal conductors, but should not be neglected as even small temperature increases will deteriorate superconductor performance, and the resulting helium boil-off and cooling expenses can be significant. The most important AC loss mechanisms are hysteresis loss arising from the irreversible magnetization behavior in type-II superconductors, and coupling loss resulting from ohmic dissipation in interfilament currents crossing the normal matrix.

The hysteretic magnetization, a characteristic of all practical type-II superconductors, is an inherent source of AC losses. When an external field H is cycled, the dissipated energy per unit volume Q depends on the induced magnetization M as [19]

$$Q = \int \mu_0 M \, \mathrm{d}H \, . \tag{31}$$

This lost energy can be interpreted as the area enclosed by the magnetization curve, such as that illustrated in Fig. 4. That is, the hysteresis loss depends only on the enclosed area and pulsing frequency; the shape of the used current waveforms is irrelevant. For a cylindrical superconductor in a transverse external field ramped from zero to B_{max} and back to zero, the integral in Eq. (31) can be evaluated to be

$$Q = \frac{8}{3\pi} B_{\mathrm{max}} J_{\mathrm{c}} a \, , \tag{32}$$

where it is assumed that the magnetization saturates at a low field and can be described by Eq. (26) with a constant critical current. This equation can be used for rough estimates of the hysteresis loss. For a more accurate calculation, the variation of J_{c} with field strength, and the effect of a possible transport current should be accounted for.

When a multifilament conductor is exposed to a changing transverse field, shielding eddy currents are induced. These current paths couple the superconducting filaments through the normal matrix, resulting in ohmic dissipation known as coupling losses. This is similar to the proximity coupling discussed in Sec. 2.2.3, except these currents decay with time instead of being truly persistent. This decay can be described with a time constant τ, similar to an LR-circuit. In an untwisted conductor, large current loops with low resistance can be found, resulting in a really large τ. Therefore, multifilament conductors are typically twisted to reduce the loop areas exposed to transverse field. In a multifilament conductor with a twist pitch p and effective transverse resistivity ρ_{t}, the coupling time constant is [22]

$$\tau = \frac{\mu_0}{2\rho_t} \left(\frac{p}{2\pi} \right)^2 \, . \tag{33}$$

For a typical AC conductor design, τ is quite small, well below 1 ms, and therefore the resulting field distortion is irrelevant in ULF-MRI use. When the field is steadily

ramped for a period long compared with τ, the dissipated power per unit volume P is [22]

$$P = \frac{2\tau}{\mu_0}\left(\frac{\mathrm{d}B}{\mathrm{d}t}\right)^2 . \tag{34}$$

The quadratic dependence on $\mathrm{d}B/\mathrm{d}t$ reveals that, unlike the hysteresis loss, the coupling loss depends on the used waveforms and can be large with ULF-MRI prepolarization pulses, which require fast ramp-downs.

To minimize the coupling loss, the wire should be twisted as tightly as possible, and the transverse resistivity should be maximized. The transverse resistivity is affected by the matrix material and the contact resistance between the matrix and the superconducting filaments. In case of a good contact, the transverse current will flow unimpeded across the filaments, reducing the effective transverse resistivity ρ_t to

$$\rho_\mathrm{t} = \rho_\mathrm{m}(1 - \lambda_\mathrm{s})/(1 + \lambda_\mathrm{s}) , \tag{35}$$

where ρ_m is the resistivity of the matrix material and λ_s the fraction of superconductor in wire [36]. In case of a bad contact the transverse resistivity is increased to [36]

$$\rho_\mathrm{t} = \rho_\mathrm{m}(1 + \lambda_\mathrm{s})/(1 - \lambda_\mathrm{s}) . \tag{36}$$

The increased ρ is often found with Nb–Ti filaments. However, this treatment with a single τ is inaccurate for more complicated composite matrices, and the precise coupling loss is best found through experiment. To increase ρ_t, a resistive matrix material can be used, such as Cu-30%Ni or Cu-0.5%Mn with resistivities 300 and 15 nΩm, respectively [34]. Typically superconductors designed for low AC losses have a composite Cu/CuNi or Cu/CuMn matrix, where the good electrical and thermal conductivity of copper is used to stabilize and protect the wire against heat releases, and the resistive material is used to suppress the proximity effect and to increase transverse resistivity.

Other than AC losses, ohmic heating in normal conductors and in joints between superconductors have to be considered. To operate the superconducting magnet in a helium bath, current has to be fed from room temperature to the coil. If this is done using copper wires, ohmic heating and helium evaporation takes place. Fortunately, the resistivity of pure copper decreases by some two orders of magnitude when cooled from room temperature to low temperatures, being 160 pΩm for oxygen-free high thermal conductivity (OFHC) copper at 4 K [21]. The resulting ohmic dissipation can be calculated simply from Joule's law $P = RI^2$. Another approach is to use high-T_c superconductor leads to supply the current, as done with the Aalto MEG–MRI device [5]. This eliminates the ohmic heating from the current leads inside the dewar. In either case, the joints between different conductors should be carefully designed and constructed, not to add excessive contact resistances.

3 Materials and methods

In this section, I will first discuss the requirements for the prepolarization coil to be used in the final ULF-MRI prototype, being built during the BREAKBEN project, and the methods used to model a superconducting prepolarization coil. Thereafter, I will propose methods to reach these requirements, and describe a test coil that was built to verify simulations of the remanent field due to coil magnetization. All numerical calculations were done in Python 3 using NumPy and SciPy packages.

A picture from the inside of the magnetically shielded room at Aalto is shown in Fig. 7. This figure shows the previous prepolarization coil made of a niobium filament conductor, as well as a helium dewar, SQUID sensor array, and the rest of the ULF-MRI coil system.

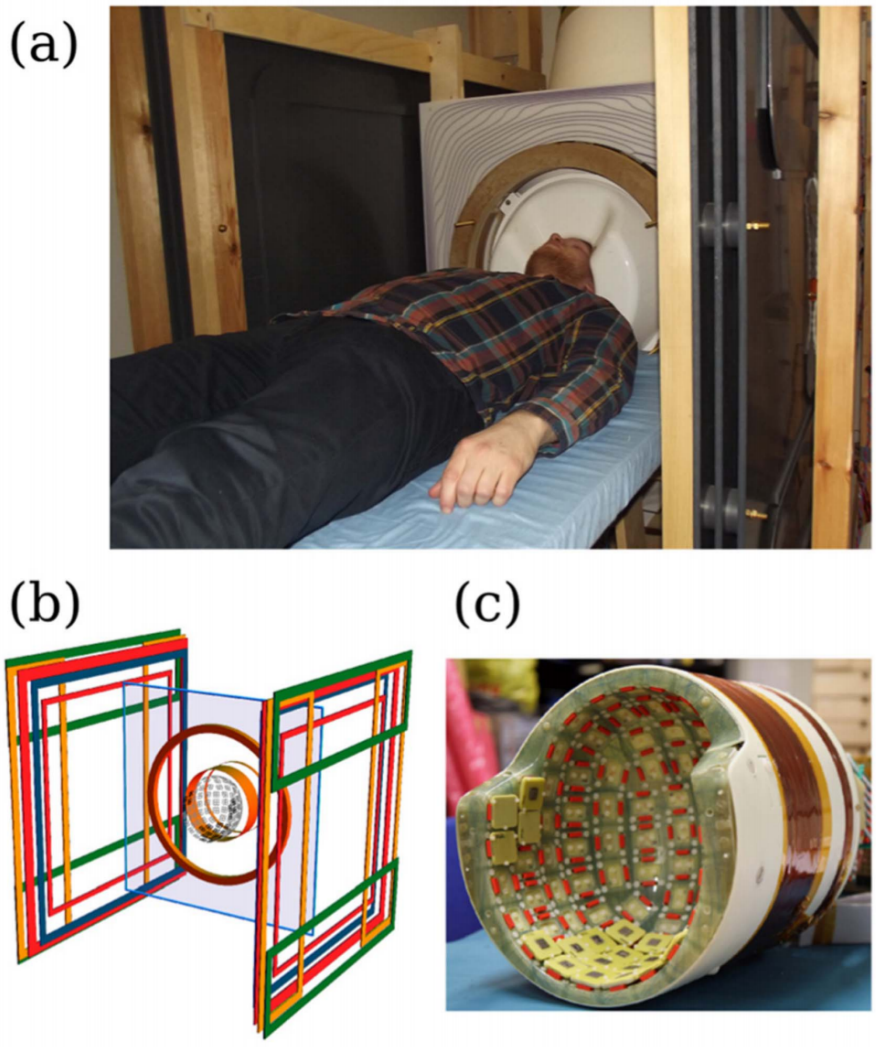

Figure 7: Parts of the Aalto MEG–MRI system, from Ref. [37]. (a) Photograph of the setup inside the magnetically shielded room. (b) Schematic of the coil system. (c) Photograph of the head-shaped SQUID-sensor array and the polarizing coil.

3.1 Field efficiency and inductance

The field efficiency, which we define as the field produced per unit current, and the inductance of the prepolarization coil affect the current and voltage requirements for driving the coil. High currents require thick conductors, which also increases the refrigeration load on the cryostat, as thick normal conductors also conduct heat into the helium dewar. The amplifier used with the prepolarization coil might for instance be capable of producing 100-A currents and 1.5-kV voltages, which is a practical balance between current and voltage. To reach e.g. a polarizing field strength of 150 mT, the field efficiency should be at least 1.5 mT/A. The current ramp-downs should be fast and controllable. To produce e.g. a 10-ms linear ramp-down with the amplifier, the inductance of the coil should be 150 mH or less.

When discussing the field efficiency, it should be remembered that the field from this type of coils will be fairly inhomogeneous in the imaging volume, and the definition of the field efficiency is not obvious. This is not a huge issue for imaging, as discussed in Sec. 2.1.3, although parts of the sample closer to the coil will give a stronger signal.

The prepolarization coil will consist of a number of coaxial circular loops of wire. This choice is because of space restrictions and for the ease of manufacture. Using more complicated coil geometries would be unlikely to give a significantly better performance. This choice makes the fields rotationally symmetric, and simplifies the following calculations.

The magnetic field produced by a number of circular loops can be found by summing the contributions from the individual loops. For a circular current loop, an analytic expression for the field produced can be found [38]. Assuming the cylindrical coordinate system (ρ, φ, z) in Fig. 8, the magnetic field from a loop of radius a carrying a current I is given by:

$$B_z = \frac{C}{2\alpha^2\beta}\left[(a^2-\rho^2-z^2)E(k)+\alpha^2K(k)\right], \tag{37}$$

$$B_\rho = \frac{Cz}{2\alpha^2\beta\rho}\left[(a^2+\rho^2+z^2)E(k)-\alpha^2K(k)\right], \tag{38}$$

where K and E are complete elliptic integrals of the first and the second kind, respectively. The following substitutions have been used:

$$C = \mu_0 I/\pi, \tag{39}$$

$$\alpha^2 = a^2+\rho^2+z^2-2a\rho, \tag{40}$$

$$\beta^2 = a^2+\rho^2+z^2+2a\rho, \tag{41}$$

$$k^2 = 1-\alpha^2/\beta^2. \tag{42}$$

The inductance of the coil can also be calculated by dividing the coil into individual loops. The total inductance L is given as the sum of the self-inductances and mutual inductances between the loops. For a coil with N turns, this becomes

$$L = \sum_{i,j=1}^{N} L_{i,j}, \tag{43}$$

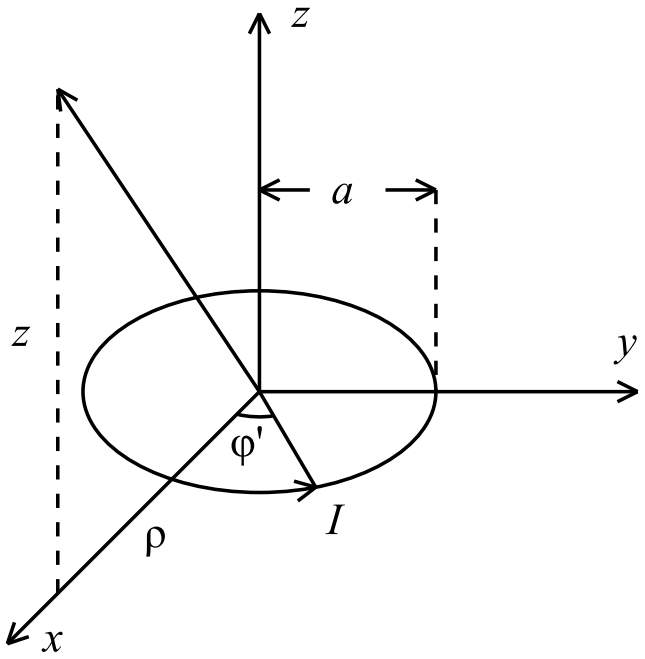

Figure 8: A single current loop in cylindrical coordinates.

where $L_{i,j}$ is the mutual inductance between loops i and j, and $L_{i,i}$ means the self-inductance of the i^{th} loop. The self-inductance of a circular loop of radius a_i, made of wire with a radius a_{w} carrying a uniform current density, can be approximated by

$$L_{i,i} = \mu_0 a_i \left(\log\left(\frac{8a_i}{a_{\text{w}}}\right) - 1.75 \right) , \tag{44}$$

when $a_{\text{w}} \ll a$ [39]. The mutual inductance between two coaxial circular loops of radii a_i and a_j, separated by distance $d_{i,j}$, is given by

$$L_{i,j} = \mu_0 \sqrt{a_i a_j} \left[\left(\frac{2}{k} - k \right) K(k) - \frac{2}{k} E(k) \right] , \tag{45}$$

where the substitution

$$k = \frac{2\sqrt{a_i a_j}}{\sqrt{(a_i + a_j)^2 + d_{i,j}^2}} \tag{46}$$

has been used [39]. This formula is also accurate for thin conductors. Therefore, combining Eqs. (43 – 45) gives a reasonable estimate for the total inductance of the coil.

3.2 Remanent magnetization

The magnetic field due to the remanent magnetization of the magnet should be low enough not to disturb ULF-MRI measurements. The remanent field is a DC or

near-DC field, and thus does not directly interfere with the measurement of NMR signal. However, it will affect the spin dynamics contributing to spin dephasing. In a typical ULF-MRI sequence, the frequency-encoding gradient field might have an amplitude of 10 μT in the imaging volume, and the frequency-encoding direction may be sampled at a resolution of 100 voxels. In this case, a field distortion of 100 nT would result in a distortion of one voxel. It would be preferable to keep the distortions below one voxel, and therefore a tolerable remanent field would be on the order of 10 nT. In case the field distortion is known, it can be compensated for in the reconstruction, relaxing the requirement for the remanent field magnitude. This type of reconstruction corrections have been studied earlier at Aalto University [40]. However, it would be preferable if the prepolarization coil allowed imaging without special attention in the reconstruction.

The remanent field component perpendicular to $\vec{B}_0$ acts to slightly rotate the total field and contributes less to the spin dephasing and image distortion. Therefore, we will mainly focus on the remanent field component parallel to $\vec{B}_0$, which directly affects the Larmor frequencies. In the intermediate and final ULF-MRI prototype setups being built during the BREAKBEN project, the axis of the prepolarization coil will be perpendicular to the $\vec{B}_0$ field. Thus, in the chosen cylindrical coordinate system (see Fig. 8), it is the radial field component B_ρ that is more important.

To simulate the magnetization and the remanent field, we will assume that the magnetization saturates during the $\vec{B}_\mathrm{p}$ pulse and can be described by Eq. (26). This is a decent approximation, as most of the coil will be exposed to fields much larger than the penetration field; for example, in a typical Nb–Ti filament with $a = 1$ μm and $J_\mathrm{c} = 20$ GA/m^2 the field penetration takes place already at $\mu_0 H_\mathrm{a} = 16$ mT, according to Eq. (27). We will also assume that the remanent magnetization is entirely due to the field from the transport current, i.e., the field produced by the magnetized nearby conductors is weak enough not to alter the magnetization. To estimate the validity of this approximation, we can calculate the average magnetization of a conductor with the same 2-μm diameter filaments and a typical superconductor fraction of $\lambda_\mathrm{s} = 0.4$. Using Eq. (26) and dividing by λ_s gives $\mu_0 M = 4.3$ mT. This is about a quarter of the penetration field, meaning there is likely some error with this approximation, depending on the geometry of the coil. More accurate modeling would be difficult and require knowledge of the magnetization behavior at fields below penetration. An example of saturated magnetization calculated using these assumptions is visualized in Fig. 9.

Within these assumptions, the remanent magnetization is given by Eq. (26) and the direction of the field produced by the transport current. Due to the axial symmetry, the conductor loops are magnetized in the transverse direction only, i.e., ρ- and z-components only. The field produced by such a magnetized loop can be calculated similarly to the field produced by a current loop. The magnetic scalar potential V_m due to magnetization $\vec{M}$, away from the source, can be written

$$V_\mathrm{m}(\vec{r}) = \int_{\mathbb{R}^3} \frac{\vec{M}(\vec{r}\,') \cdot (\vec{r} - \vec{r}\,')}{4\pi \left|\vec{r} - \vec{r}\,'\right|^3} \,\mathrm{d}r'^3 \,, \tag{47}$$

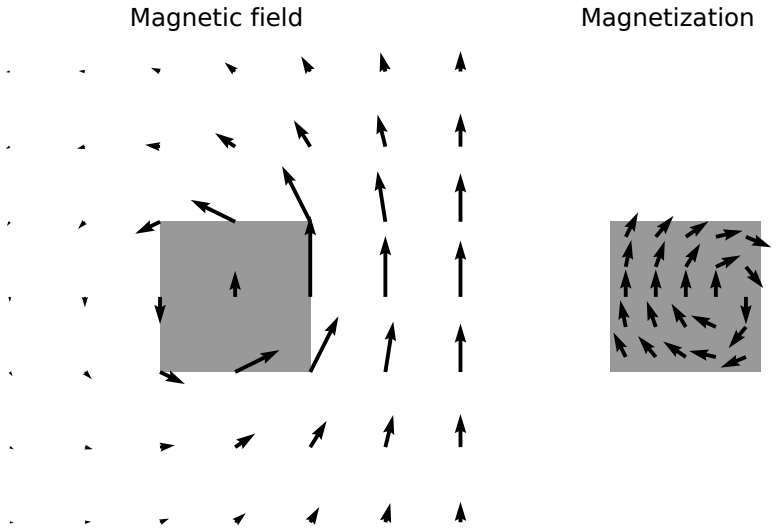

Figure 9: The magnetic field produced by the transport current and the saturation magnetization in a short solenoid coil. The gray areas denote the coil cross-section, which consist of a number of conductors.

where the primed coordinates refer to the source and the unprimed coordinates to the position where V_m is evaluated. Assuming a small, circular wire cross-section of radius a_w, the magnetization of a loop in the $z = 0$ plane can be written with Dirac delta functions

$$\vec{M}(\vec{r}\,') = (M_z \hat{e}_z + M_\rho \hat{e}_\rho)\, \pi a_\mathrm{w}^2 \delta(z')\delta(\rho' - a)\,, \tag{48}$$

using the cylindrical coordinates in Fig. 8. The distance between the source and the field point is

$$|\vec{r} - \vec{r}\,'| = \sqrt{z^2 + \rho^2 + \rho'^2 - 2\rho\rho' \cos\varphi'}\,. \tag{49}$$

Combining Eqs. (47 – 49) and integrating over the delta functions gives

$$V_\mathrm{m}(\vec{r}) = \frac{a^2\rho}{4} \int_0^{2\pi} \frac{M_z z - M_\rho a + M_\rho \rho \cos\varphi'}{(z^2 + \rho^2 + a^2 - 2a\rho\cos\varphi')^{3/2}}\, \mathrm{d}\varphi'\,. \tag{50}$$

This integral has an analytic solution containing elliptic integrals, as was found using Wolfram Mathematica. The Mathematica code is shown in Appendix A. To model the remanent field of a coil, the contributions to V_m from the different turns can be summed, and finally, the magnetic field can be found by differentiating

$$\vec{B}(\vec{r}) = -\mu_0 \nabla V_\mathrm{m}(\vec{r})\,. \tag{51}$$

3.3 Coil design

The prepolarization coil previously used in the Aalto ULF-MRI setup is made of a niobium conductor, in an effort not to exceed the lower critical field H_{c1}, where the vortices first penetrate, and this way avoiding the problem with remanent magnetization. For this purpose, the coil has the shape of a thin solenoid (see Fig. 7c), where the maximum field at the coil can be kept reasonably low. However, for prepolarizing fields exceeding 100 mT, staying below H_{c1} will no longer be possible, and not exceeding H_{c2} would be difficult as well, regardless of the choice of materials. Reaching the higher fields requires a strongly type-II material, with a large H_{c2} and consequently a low H_{c1}. This inevitably leads to some remanent magnetization, and therefore the approach chosen is to use a conductor with a low remanent magnetization and a coil geometry where the field due to this magnetization is minimized.

3.3.1 Coil geometry

The geometry of the coil affects all relevant properties of the coil, such as the fields produced, inductance, field efficiency, and mechanical stresses from the Lorenz forces. The magnetic field produced by the remanent magnetization has proven to be a great issue for ULF MRI, and therefore the design proposed focuses on minimizing this secondary field. The design chosen is a tightly wound current loop. To see the motivation for such a design, we can consider a straight infinitely long bundle of conductors with a circular cross-section, as shown in Fig. 10. The field produced by this bundle of conductors carrying a total transport current I, evenly shared by the individual conductors, is entirely azimuthal, leading to an azimuthal magnetization as well. Such a magnetization corresponds to a bound surface current, and an equal amount of bound volume current in the opposite direction. Due to the symmetry of the conductor, these bound currents produce no magnetic field outside the conductor. Worth noting here is also that as the current is ramped down, the magnetic field has contributions from both the transport current and the magnetization. However, these fields are parallel due to the symmetry, and thus the direction of the magnetic field and the result of no external remanent field remain unchanged. Unfortunately, such geometry is not possible with magnets that always consist of loops of wire. However, as the cross-section of the coil is made smaller while keeping the diameter constant, we can approach the case where the field near the conductors is that created by an infinitely long and straight conductor.

To validate this design approach, a small test coil was constructed. This test coil is designed to fit inside a small helium dewar with a 160-mm diameter cylindrical helium volume, that will also house the intermediate prototype. The final MEG–MRI prototype to be constructed later in the BREAKBEN project is able to house a larger, about 300-mm diameter prepolarization coil. This larger diameter gives a magnetic field near the coil closer resembling that of an infinite conductor, and therefore the same design approach can be expected to work with the final prototype, if the test coil proves to be successful.

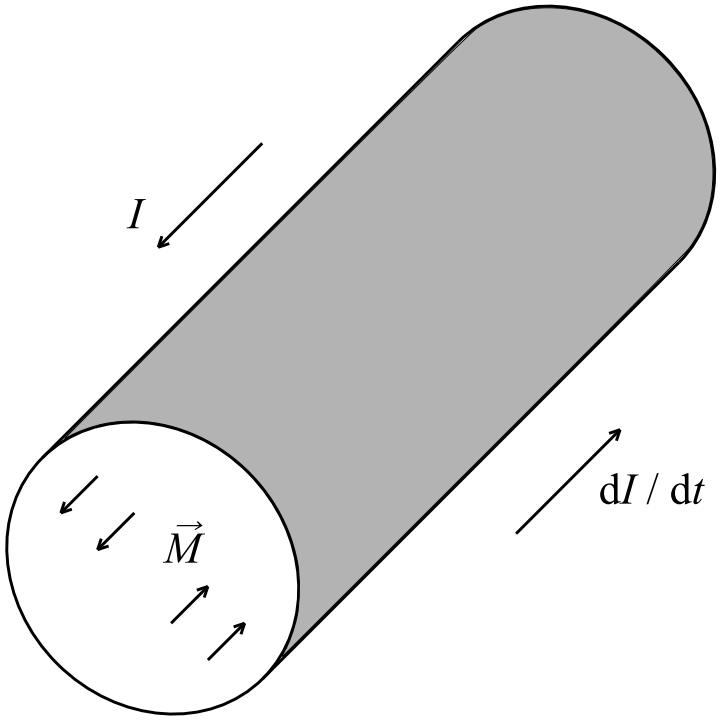

Figure 10: The magnetization in an infinitely long and round conductor bundle, after the total transport current has been ramped down to I from a much larger value.

For easier realization of the test coil, the cross-section is chosen to be rectangular. The outer diameter of the coil is chosen to be 140 mm, and the number of turns is chosen to be 600, giving a total conductor length of 275 m. The cross-section becomes a 6 mm wide by 4 mm thick rectangle, assuming a 0.2-mm conductor in a square lattice. Later on, it was found that the coil turned out slightly thicker at about 5 mm, and therefore the following calculations are done using a correspondingly lower packing density. Performing the calculations described in Sec. 3.1, we find an inductance of 114 mH and a field efficiency of 2.8 mT/A on the coil axis at a 20-mm distance from the bottom of the dewar, when the coil is lowered to the bottom of the helium volume. The field produced by the transport current is visualized in Fig. 11. The maximum field the conductor is exposed to is 43 mT/A. In case this coil is used with the intermediate ULF-MRI setup, the distance between the coil and the bottom of the dewar needs to be increased by some centimeters to make room for the SQUID sensors.

3.3.2 Choice of the superconducting wire

The choice of the superconducting wire is critical for the low remanent magnetization requirement and low AC losses, as well as for sufficient current density and stability. To

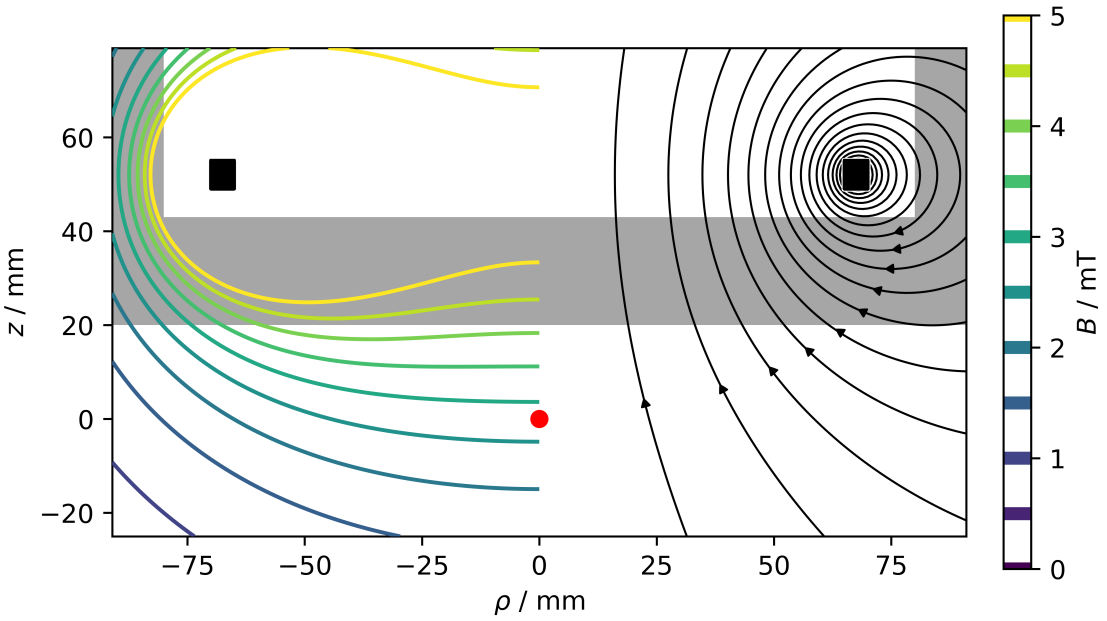

Figure 11: The magnetic field produced by the transport current in the test coil. The left side shows the magnitude of the field, while the right side shows field lines. The gray area denotes the cross-section of the helium dewar, and the red dot is the point at which the field efficiency is defined.

achieve the low remanent magnetization, fine filaments are required as the saturation magnetization scales linearly with the filament diameter (Eq. (26)). According to the following simulations, a filament diameter on the order of 1 μm is needed to reach remanent fields below 10 nT. The finer the filaments, the lower the remanent field, as long as the proximity coupling does not significantly increase the magnetization, which will be an issue with filament diameters much below 1 μm. In addition, the manufacturability and availability will constrain the choice of the superconductor.

The AC losses in the conductor should be low enough not to cause too much helium boil-off, and not to excessively heat the conductor lowering the critical current. The most important loss mechanisms are hysteresis and coupling losses, as discussed in Sec. 2.3.3. The choice of fine filaments is also useful to reduce the hysteresis losses, as the field is cycled. However, the extremely fast field ramp-downs are demanding in terms of the coupling losses as well. For low enough coupling losses, a tight twist pitch and a high transverse resistivity is required to have a sufficiently low coupling time constant.

A suitable conductor with fine filaments and low AC losses was not found readily available. Instead, we used a standard filamentary Nb–Ti conductor with 54 filaments dispersed in a pure copper matrix. The wire has a type number 54S43, and is manufactured by Supercon Inc. At 0.178-mm diameter, the filament diameter is 14.8 μm, and the overall wire diameter including the insulation is 0.203 mm. The twist pitch of the conductor is 22.1 mm. It is expected that the AC losses with this coil are significant and that it may not be suitable for repeated pulsing. It is also unlikely that the remanent field below the coil could be lowered below 10 nT for a very large volume. However, this coil allows us to test remanent field cancellation methods, and to compare them against the simulations. Therefore, this coil should be useful in assessing whether this approach is suitable for upscaling to a larger prepolarization coil made of a more suitable, possibly custom-manufactured conductor.

To estimate the effect of the AC losses in the test coil, we can calculate the losses as described in Sec. 2.3.3. During a 30-A pulse, the coil is exposed to a 1.2-T maximum, 0.82-T RMS, and a 0.77-T average self-field over the different turns of wire. The critical current is taken to be 5 GA/m^2, and the transverse resistivity to be that of OFHC copper 160 pΩm. The volumetric heat capacity is taken to be 5 kJ/m^{3}K, which roughly represents the material properties of the windings at temperatures near 4.2 K [22]. The hysteresis loss is independent of the ramp durations and pulse amplitude, and can be calculated using Eq. (32). Assuming there is no heat conduction during a fast ramp-down, i.e., adiabaticity, the temperature increase due to hysteresis loss becomes 0.8 K. If the magnet is pulsed at a 1-Hz frequency, the liquid helium boil-off rate due to hysteresis becomes 0.12 l/h, using a volumetric evaporation heat of 2.5 kJ/l for liquid helium [21]. These are rough estimates, but it appears that neither the boil-off rate or the adiabatic temperature increase due to hysteresis should be a major issue, although for economical usage and optimal performance, such losses should not be neglected. These losses could be easily reduced by choosing a conductor with finer filaments. The coupling loss is dependent on the ramp durations and field amplitude, and can be calculated using Eqs. (32 and 33). The ramp-up can be made much longer than the ramp-down, and therefore the

coupling losses will be dominated by the fast ramp-down. For a single 10-ms ramp-down, the heat released can be calculated to be 41 J. Such a heat release is more than enough to heat the winding to the critical temperature 9.8 K. Fortunately, the heat increase in a fast ramp-down is limited to the critical temperature, as the loss of superconductivity also destroys the coupling loss mechanism. During longer ramp-downs, the losses are smaller, and the heat can be better dissipated by the boiling helium. Therefore, fast $\sim$ 10 ms ramp-downs are probably not possible without strong helium evaporation, but slower ramp-downs can be used for testing purposes. In case the magnet is heated to the critical temperature 9.8 K during each pulse, the helium boil-off rate with 1-Hz pulsing becomes a costly 1.1 l/h, using a specific enthalpy of 60 kJ/m^3 at 9.8 K, representative of a typical winding [22]. Decreasing the twist pitch and using a resistive matrix would be effective in reducing these coupling losses.

The remanent field for the test coil was simulated as described in Sec. 3.2 using the parameters of the 54S43 conductor. The resulting field pattern and the magnitude of the radial field is visualized in Fig. 12a. This figure shows that the component of the remanent field parallel to $\vec{B}_0$ well exceeds 100 nT below the dewar, which would result in unacceptable field distortions. Methods for further lowering this remanent field to acceptable levels are discussed in the following sections.

3.3.3 Passive superconductor turns

Further examining the magnetization of the coil shown in Fig. 9, we can see that the radial magnetization is anti-symmetric about the mid-plane of the coil, having an equal amount of magnetization in the inward and outward directions. However, in the axial direction such a balance is absent, and the coil has a net magnetic moment in this direction. This imbalance will increase the field produced away from the coil, and should be minimized.

It is possible to achieve cancellation of the remanent field by adding material that becomes magnetized during the operation of the magnet. This material contributes to the remanent field, and by carefully placing this material around the superconducting magnet itself, reduction of the remanent field is achieved. This type of cancellation has been suggested earlier, using pieces of passive superconductor, ferromagnetic material, or oriented permanent magnet material [41, 42]. This is also similar to passive shimming of a traditional MRI magnet, which is commonly done using ferromagnetic materials [1]. Turns of passive superconductor is the chosen method in this study. This has the advantage that the same conductor can be used as in the main coil, and even if the magnetization of the conductor is not exactly known, it should be closely the same in the main coil and in the passive turns. In addition, with ferro- or ferrimagnetic materials, there is a possibility of introducing a new problem with Barkhausen noise.

Ideally, the number and location of the passive turns should be optimized to minimize the remanent field inside a chosen imaging volume. Finding the optimum would, however, require very accurate modeling of the remanent field. For the test coil design, it was calculated that 60 passive turns evenly laid on the outside surface

of the coil should reduce the dipole moment of the magnet close to zero. The even layer of turns should also be easily implemented. The simulated remanent field for the coil with 60 passive turns is shown in Fig. 12b. This reveals that there is, at least theoretically, a significant reduction in the remanent field compared to the coil without passive turns. However, the remanent field is sensitive to other external fields and imperfections in the winding, and therefore this reduction cannot be realized in full. Especially, applying $\vec{B}_0$ and gradient fields is expected to have an effect in the remanent field produced. In case the coil is to be operated together with shielding coils to reduce the stray field, this should be considered in the design of the passive winding, as it will affect the need for passive turns.

3.4 Defluxing

So far, we have only discussed how to reduce the saturation magnetization following a simple trapezoidal $\vec{B}_\mathrm{p}$ pulse. However, it is also possible to further reduce the remanent field of the magnet by using a current waveform designed to reduce the remanent magnetization. This method will be useful for our purposes in case the field due to the saturated magnetization needs to be further reduced.

The idea of defluxing is to use a decaying AC current, during which vortices of opposing directions can penetrate into the superconductor, and the remanent field can be made weaker. When two vortices of opposing directions are brought close to each other, there is a mutual attraction, and it is even possible for the vortices to annihilate if they meet. This type of defluxing has been successfully used also for defluxing SQUID sensors [43, 44] and pick-up loops [45].

A long slowly decaying waveform is likely to be effective in defluxing. However, for in-sequence defluxing, the waveform should be short to allow measurements to be started soon after the polarizing pulse. In addition, the resulting AC losses may constrain the possible waveforms. Short and effective defluxing can be achieved by adding an oscillating tail to the prepolarizing current waveform, defined by a few parameters, and experimentally optimizing the parameters. This type of DynaCAN defluxing has been studied earlier as well [46, 47]. A possible DynaCAN defluxing waveform with two parameters is shown in Fig. 13.

The drawback with using defluxing tails in $\vec{B}_\mathrm{p}$ pulses is that some delay may be added between the beginning of the $\vec{B}_\mathrm{p}$ ramp-down and the start of the signal acquisition. However, the temporal profile of the waveforms should not be very important, and small oscillations can be done in quite short time windows. Matlashov *et al.* [43] did not notice obvious frequency dependencies with $3 - 30$ kHz carrier frequencies. During the defluxing waveform it is in principle possible to deflux other superconducting parts of the MEG–MRI system as well, such as pick-up coils.

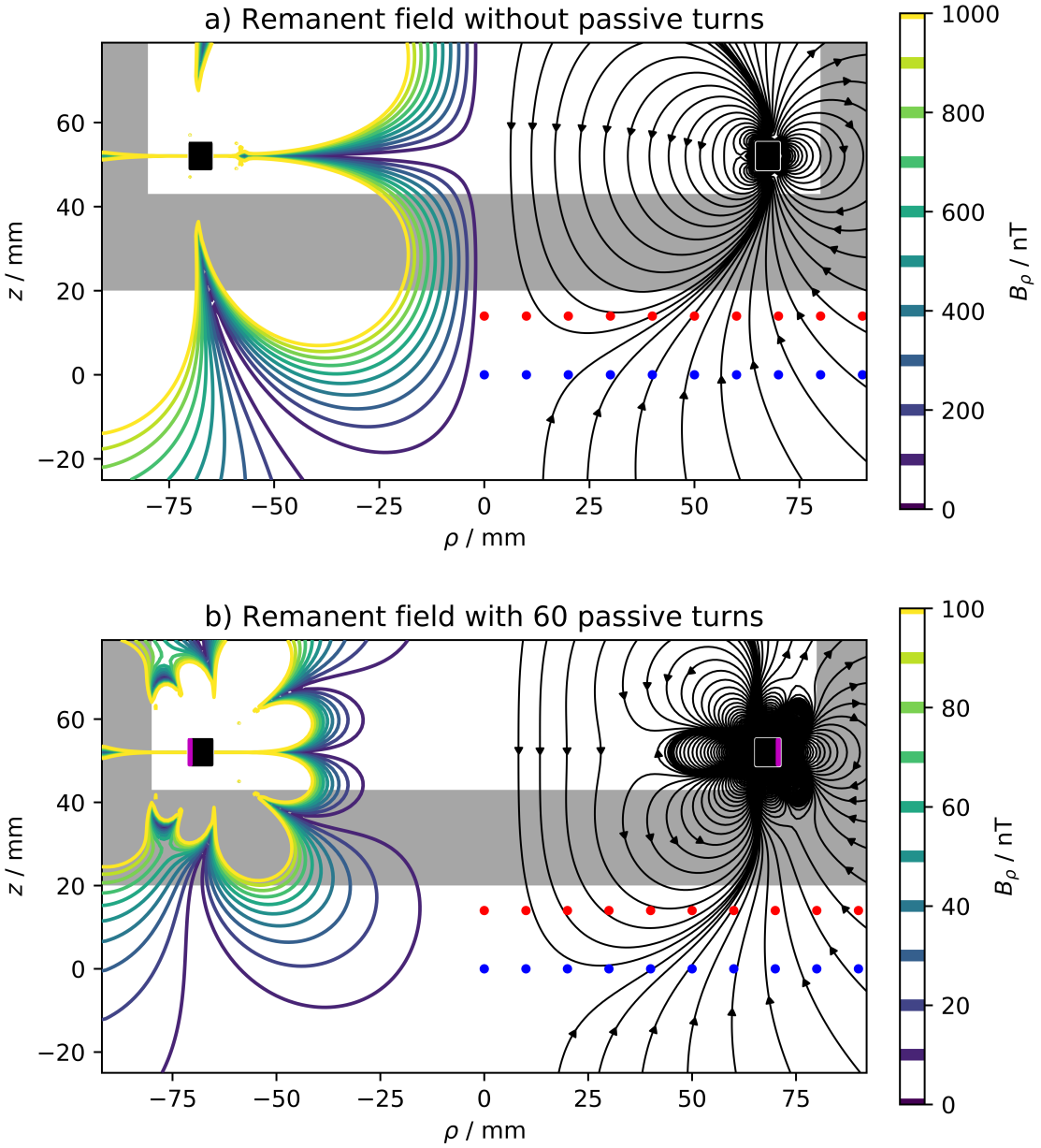

Figure 12: The magnetic field produced by the remanent magnetization in the test coil without (a) and with (b) passive turns (colored purple). The left side shows the magnitude of the radial component of the field, while the right side shows field lines. The gray area denotes the cross-section of the helium dewar. The locations for the experimental field measurements are indicated by the red (B_ρ) and blue (B_z) dots.

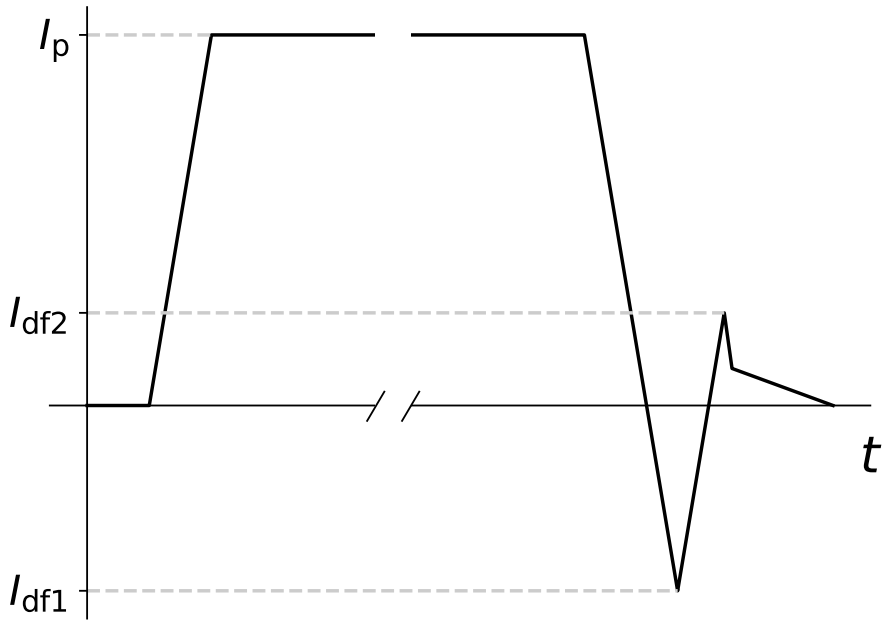

Figure 13: A prepolarization pulse current waveform with a DynaCAN tail designed to deflux the superconducting coil. I_{df1} and I_{df2} are the free parameters that can be optimized for effective defluxing. The slow ramp at the end is used to ensure an adiabatic $\vec{B}_{\mathrm{p}}$ turn-off.

4 Results

4.1 Coil implementation

The test coil design described in Sec. 3.3 was realized by wet-winding the 54S43 superconductor onto a bobbin made of cotton reinforced phenolic sheets. The used impregnating resin was Emerson-Cumings Stycast 2850FT cryogenic epoxy, which is designed for low thermal expansion and good thermal conductivity. The winding was applied using an automated winding machine, which resulted in a fairly even layup throughout the winding. The thickness of the coil was measured to be approximately 5 mm, corresponding to a packing density slightly below that of a square lattice, which would have given a 4-mm coil thickness. The leads of the coil were soldered to 2.5-mm^2 copper conductors using 60/40 Sn–Pb solder. The finished coil is shown in Fig. 14.

At room temperature, the resistance of the coil was measured to be 320 Ω. The inductance of the coil was measured using an Escort ELC-130 LCR-meter, giving 105 mH. Calculating the inductance of the test coil as described in Sec. 3.1 gives an inductance of 114 mH. This difference between theory and measurements is most likely due to approximations in the inductance calculation, and possible measurement error. There is also some uncertainty in the wire packing density, but this does not completely explain the discrepancy.

The critical current was tested by pulsing the magnet with variable amplitude current pulses with a 2-s linear ramp-up. The amplitude was increased in 1-A steps, and the coil was first observed to quench with a 38-A pulse. Therefore, the critical current is at least $I_\mathrm{c} = 37$ A, corresponding to a reasonable critical current density $J_\mathrm{c} = 3.4$ GA/m^2 for the Nb–Ti filaments. At such current, the maximum field the superconductor is exposed to is calculated to be approximately 1.5 T.

4.2 Remanent field measurements

To measure the remanent field, the current in the coil was pulsed using a Kepco BOP-36-12M amplifier, after which the field below the coil was measured using a Bartington Mag-03MC1000 3-axis fluxgate magnetometer. During the measurements, the current source was disconnected from the coil using electromechanical relays to prevent the noise from the current supply from interfering with the measurements. To study the effect of the passive turns, the coil was first wound with 50 passive turns. The measurements suggested that adding some more passive turns could provide a better cancellation, and 10 more turns were added. The 60 passive turns indeed provided a larger area where the field could be reduced below 10 nT, and therefore the measurements with the 60 passive turns are reported in more detail below.

First, the coil was zero-field cooled and the axial field on the axis of the coil was measured after pulses of increasing amplitude. The distance between the center of the coil and the fluxgate sensor was 52 mm. The current pulses were trapezoidal with ramp-up and ramp-down durations of 0.9 s. The amplitude of the pulses was increased from zero to 20 A in 19 steps. This measurement was repeated after the

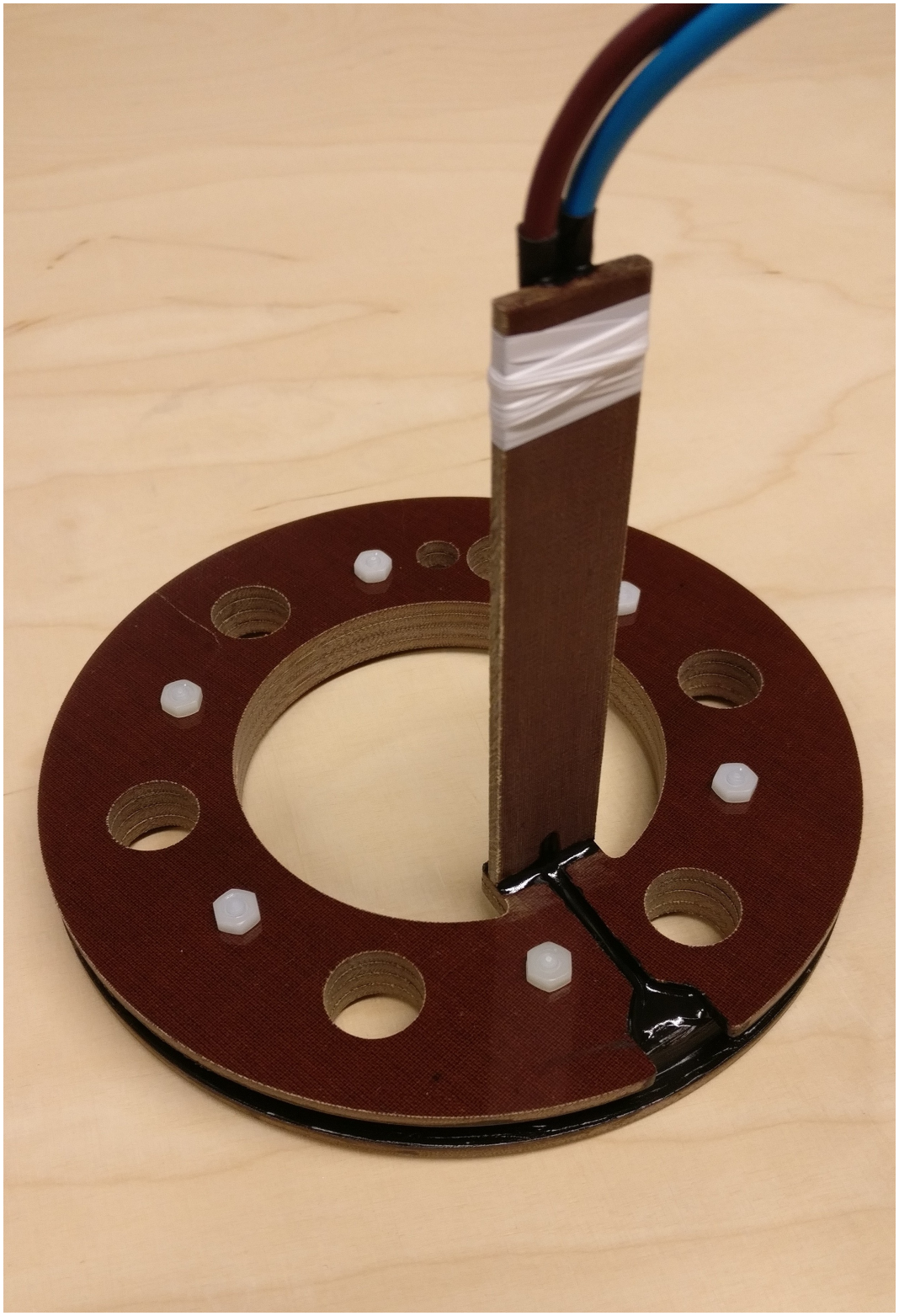

Figure 14: The test coil was constructed by wet-winding 600 turns of superconductor onto a bobbin made of cotton-reinforced phenolic.

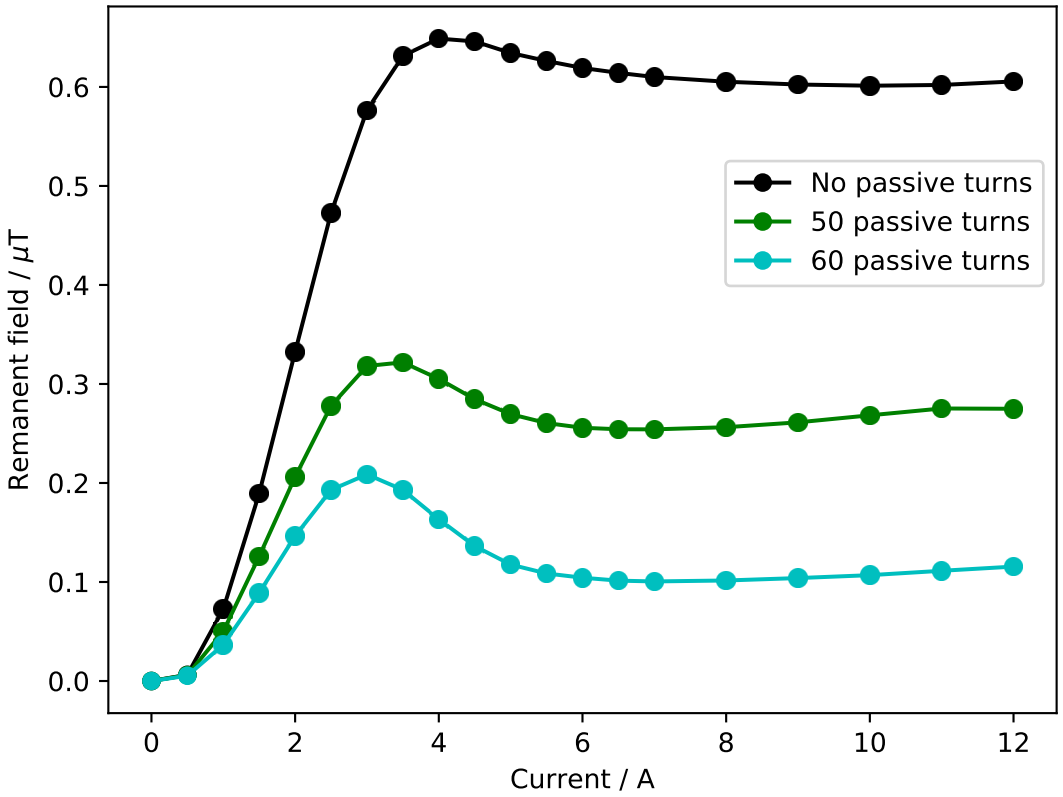

Figure 15: The axial remanent field on the axis of the coil after zero-field cooling and current pulses of varying amplitude.

passive turns had been added to the coil. The results are shown in Fig. 15. This figure clearly shows the saturation of the remanent field, meaning that the 12-A current source is sufficient for these studies. Here it can already be seen that the passive turns can effectively reduce the remanent field.

After the magnetization of the coil had been saturated with the 12-A pulse, the radial dependence of the remanent field was mapped by moving the fluxgate sensors radially from the axis of the coil $\rho = 0$ mm to $\rho = 90$ mm in 10-mm steps. The Mag-03MC1000 3-axis fluxgate magnetometer has three orthogonal sensors at slightly different locations. Two of these sensors were aligned with the radial and axial components of the remanent field, as the sensors were moved right below the dewar. The points at which the field components were measured are illustrated in Fig. 12. The results with a coil having no passive turns, and a coil with 60 passive turns are shown in Fig. 16.

The addition of 60 passive turns reduced the remanent field over the measurement range by an order of magnitude. Without the passive turns, the level of the remanent field is totally unacceptable for ULF-MRI use. However, with the addition of 60 passive turns, we find that the measurements of the radial remanent field at $\rho \leq 30$ mm stay below 10 nT.

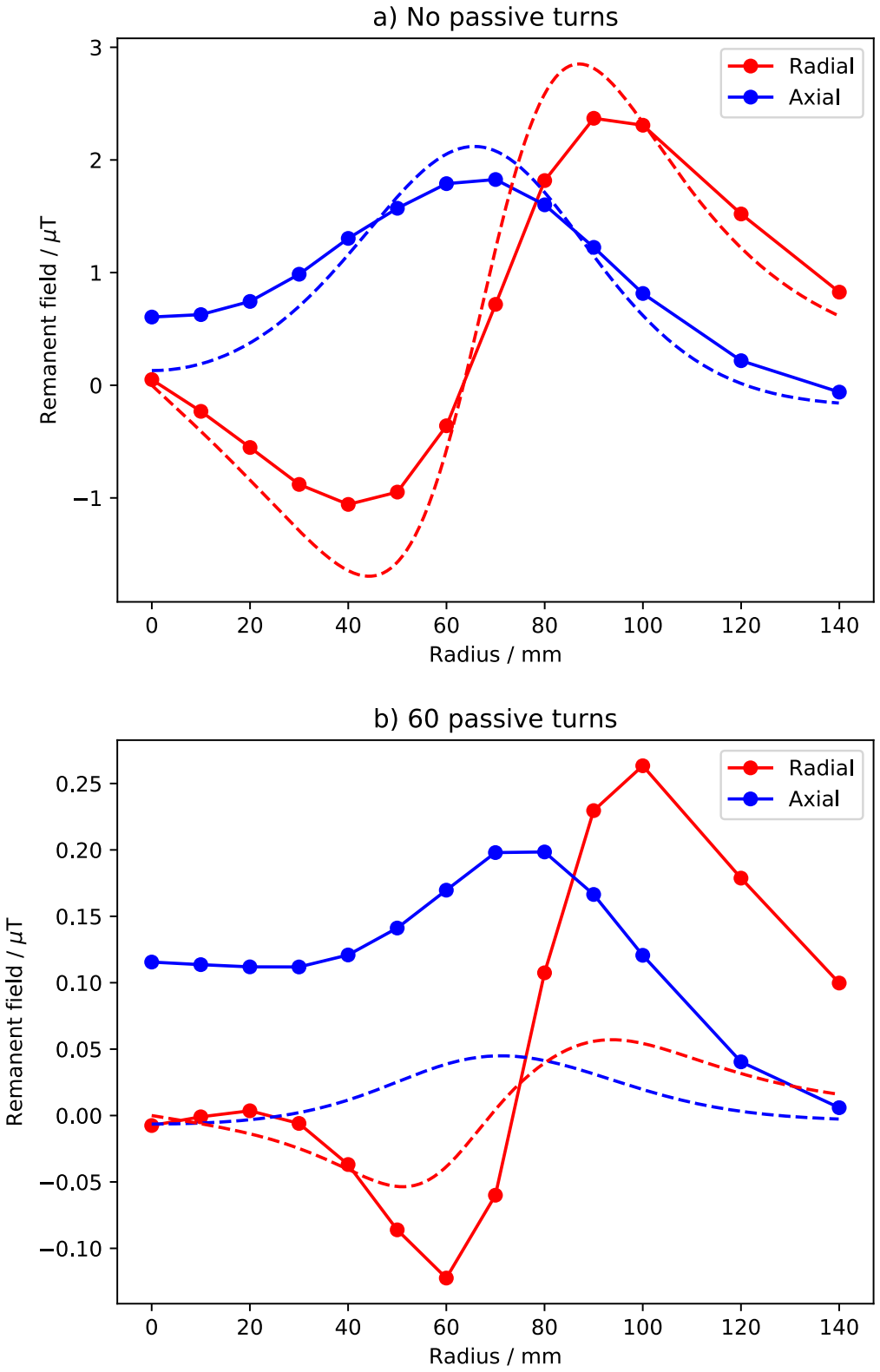

Figure 16: The remanent field measured at different radial positions after the magnetization has been saturated by a 12-A current pulse. The dashed lines show the predictions of the simulations.

The predictions of the simulations are also plotted in Fig. 16. It can be seen that with no passive turns, the simulations quite well match the measurements, although there are errors on the order of 100 nT. With 60 passive turns, the absolute error of the simulation is no larger than with no passive turns, but the relative error becomes larger and the simulations no longer have a very good match with the measurements. This kind of errors have been expected, as there are multiple error sources in the simulation, including the approximation of fully saturated magnetization, geometrical mismatch between the simulated and the constructed coil, and uncertainty of material parameters, such as the critical current. Simulating a coil with accurately cancelled remanent field is more difficult, as the details of the magnetization become more important.

4.3 Defluxing

Defluxing of the coil was studied using a simple waveform, where the polarizing pulse is followed by a single counterpulse. The test coil without passive turns was first pulsed with 12 A to reach the saturation magnetization, followed by an opposite counterpulse, whose amplitude was varied from 1.2 A to 1.7 A in 0.1-A increments. The remanent field after the different defluxing pulses was measured at different radial positions, the positioning of the fluxgate magnetometer again being the same as visualized in Fig. 12. These measurements are presented in Fig. 17, showing that a counterpulse with 1.4-A amplitude is quite effective in reducing the radial magnetization. Comparing Fig. 17 with Fig. 16a reveals that the simple 1.4-A counterpulse has reduced the radial field by some two orders of magnitude.

Using a more complicated defluxing waveform, such as that shown in Fig. 13 with two field oscillations, should give further reduction of the remanent field. Optimizing the longer waveforms is, however, quite time consuming. Measuring the remanent field of a coil that has been thoroughly defluxed requires also great care to ensure that measurement errors, such as the fluxgate offset or fields from other nearby magnetized materials, do not significantly affect the results. For these reasons, longer waveforms were not studied.

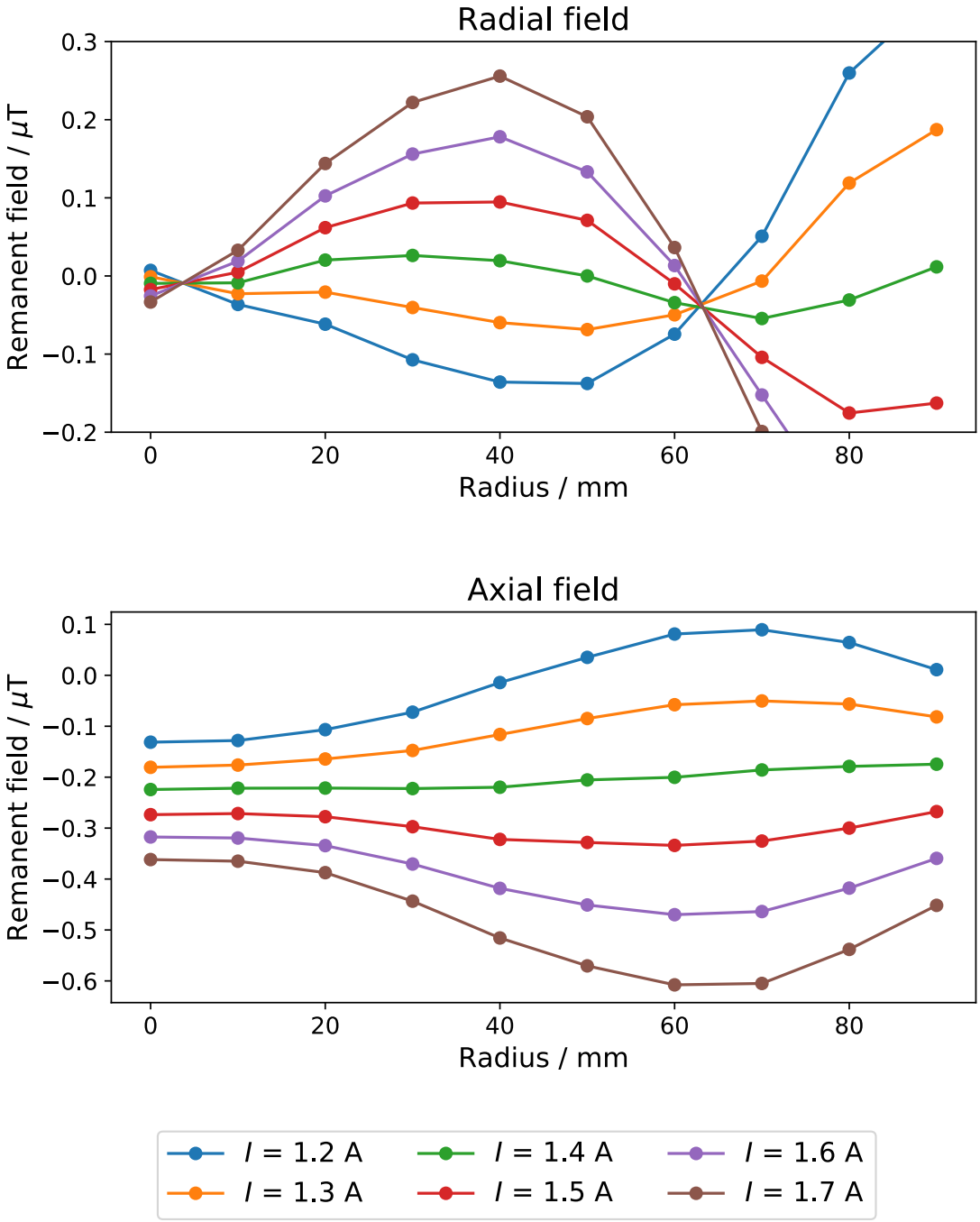

Figure 17: The remanent field measured at different radial positions after simple defluxing pulses with different amplitudes.

5 Conclusions and discussion

In this thesis, the possibility of constructing an improved superconducting prepolarization electromagnet for ULF MRI was investigated. The emphasis was on increasing the available $\vec{B}_\mathrm{p}$ field strength without increasing the produced remanent field after a strong current pulse. The mechanisms affecting the remanent field and possible cancellation methods are investigated. In addition, other engineering aspects, such as AC losses and mechanical design, are discussed. Finally, a test coil was constructed to experimentally verify the field simulations.

The challenges with field distortion stem from the fact that superconductors are magnetized in external fields, which is their intrinsic property. In low fields, all superconductors with dimensions greater than the London penetration depth behave as perfect diamagnets, completely expelling external fields. Superconductors suitable for high-field applications also display flux penetration in the form of magnetic vortices, above the material's first critical field. These vortices are pinned into defects in the superconductor, resulting in a hysteretic behavior of the magnetization, also known as flux trapping. Choosing materials with weak flux pinning does not help, as flux pinning is also the mechanism allowing the high current densities in superconducting wires. The requirements are demanding, as the remanent field should be on the order of 10 nT to avoid significant field distortion, while a polarizing field exceeding 100 mT is our goal.

Previously, at Aalto University, a superconducting prepolarization coil made of a conductor with pure niobium filaments has been successfully used. This is a unique approach to superconducting coil design, where the problem of remanent magnetization can be avoided by operating the coil below the first critical field of niobium, altogether preventing vortex nucleation. However, with a desire to reach a stronger prepolarization field, this approach is no longer possible. The niobium coil at Aalto is limited to field strengths up to 22 mT without vortex nucleation, and fields up to 60 mT without quenching. There are no known materials that would allow this approach to be scaled up to field strengths above 100 mT.

To realize an improved superconducting prepolarization coil, the approach proposed is to use a multifilament superconductor with low remanent magnetization, and combine this with a coil geometry that minimizes the external field produced by the magnetized conductors. This alone is likely not sufficient in reducing the remanent field to a tolerable level. To further reduce the remanent field, we studied the addition of passive turns and the use of defluxing current waveforms. Passive turns consist of superconducting wire that does not carry the transport current, but is still magnetized by the field it produces. By correctly placing these passive turns, the remanent field can be reduced, similar to the shimming of a traditional MRI magnet, which is commonly done using ferromagnetic materials. Defluxing current waveforms mean current pulses with fluctuating tails, which can be used for shaping the magnetization of the coil. Defluxing waveforms should allow a very high level of remanent field reduction, which can be tuned in software for different coils and ULF-MRI setups. However, this comes at the cost of some time delay and increased AC losses. In addition, defluxing requires a current supply capable of performing

the fast current oscillations. The use of passive turns can also offer a good level of remanent field reduction, and is less demanding on the current supply, but the fine tuning of the passive turn winding can be difficult and time consuming. With the test coil, we were able to reduce the remanent field after a strong current pulse to tolerable levels over a small volume using both the passive turns without defluxing, and simple defluxing waveforms without passive turns. This is a successful result, considering that the overall dimensions of the test coil are quite small and that it was constructed using a suboptimal conductor. The test coil could possibly be used in preliminary ULF-MRI tests as well. Other external fields, such as $\vec{B}_0$, likely have some effect on the remanent field, and this should still be further studied.

To provide some guidance in the design process, the remanent field of a prepolarization coil was simulated. Accurately modeling the magnetization of thin superconductor filaments is difficult, and some approximations were made, including that all parts of the coil are fully saturated. Comparisons with the experimental results show that the simulation fairly well matches the measured remanent field from the test coil without passive turns. However, when passive turns are used to cancel most of the remanent field, the relative error of the simulation significantly increases, which is expected, as here the details of the remanent magnetization become important. This means that the fine tuning of the number of passive turns is best done experimentally.

The results obtained in this work are promising in that a superconducting prepolarization coil producing a field exceeding 100 mT with insignificant image distortion could be realized. We demonstrated methods that allow the remanent field to be reduced to tolerable levels, using the test coil. The construction of a superconducting prepolarization coil for ULF MRI will require a carefully chosen conductor, with a low saturation magnetization and low AC losses. However, a suitable conductor was not readily available. Therefore, the choice of the superconducting wire needs to be further investigated before manufacturing a prepolarization coil for the final ULF-MRI prototype. This may require custom-manufacturing.

References

[1] R. W. Brown, Y.-C. N. Cheng, E. M. Haacke, M. R. Thompson, and R. Venkatesan, *Magnetic Resonance Imaging: Physical Principles and Sequence Design*. New Jersey: John Wiley & Sons, second ed., 2014.

[2] Z.-P. Liang and P. C. Lauterbur, *Principles of Magnetic Resonance Imaging: A Signal Processing Perspective*. New York: IEEE Press, 2000.

[3] J. Clarke, M. Hatridge, and M. Mößle, "SQUID-detected magnetic resonance imaging in microtesla fields," *Annual Review of Biomedical Engineering*, vol. 9, pp. 389–413, 2007.

[4] R. H. Kraus Jr., M. A. Espy, P. E. Magnelind, and P. L. Volegov, *Ultra-Low Field Nuclear Magnetic Resonance: A New MRI Regime*. New York: Oxford University Press, 2014.

[5] P. T. Vesanen, J. O. Nieminen, K. C. J. Zevenhoven, J. Dabek, L. T. Parkkonen, A. V. Zhdanov, J. Luomahaara, J. Hassel, J. Penttilä, J. Simola, A. I. Ahonen, J. P. Mäkelä, and R. J. Ilmoniemi, "Hybrid ultra-low-field MRI and magnetoencephalography system based on a commercial whole-head neuromagnetometer," *Magnetic Resonance in Medicine*, vol. 69, no. 6, pp. 1795–1804, 2013.

[6] S. Hartwig, J. Voigt, H. J. Scheer, H. H. Albrecht, M. Burghoff, and L. Trahms, "Nuclear magnetic relaxation in water revisited," *Journal of Chemical Physics*, vol. 135, no. 5, 2011.

[7] P. T. Vesanen, J. O. Nieminen, K. C. J. Zevenhoven, Y. C. Hsu, and R. J. Ilmoniemi, "Current-density imaging using ultra-low-field MRI with zero-field encoding," *Magnetic Resonance Imaging*, vol. 32, no. 6, pp. 766–770, 2014.

[8] J. O. Nieminen, K. C. J. Zevenhoven, P. T. Vesanen, Y. C. Hsu, and R. J. Ilmoniemi, "Current-density imaging using ultra-low-field MRI with adiabatic pulses," *Magnetic Resonance Imaging*, vol. 32, no. 1, pp. 54–59, 2014.

[9] M. H. Levitt, *Spin Dynamics: Basics of Nuclear Magnetic Resonance*. Chichester: John Wiley & Sons, second ed., 2008.

[10] R. McDermott, S. Lee, B. ten Haken, A. H. Trabesinger, A. Pines, and J. Clarke, "Microtesla MRI with a superconducting quantum interference device," *Proceedings of the National Academy of Sciences of the United States of America*, vol. 101, no. 21, pp. 7857–7861, 2004.

[11] V. S. Zotev, A. N. Matlashov, P. L. Volegov, A. V. Urbaitis, M. A. Espy, and R. H. Kraus Jr., "SQUID-based instrumentation for ultralow-field MRI," *Superconductor Science and Technology*, vol. 20, no. 11, pp. S367–S373, 2007.

[12] J. Clarke and A. I. Braginski, *The SQUID Handbook: Fundamentals and Technology of SQUIDs and SQUID Systems*, vol. 1. Weinheim: Wiley-VCH, 2005.

[13] J. Luomahaara, P. T. Vesanen, J. Penttilä, J. O. Nieminen, J. Dabek, J. Simola, M. Kiviranta, L. Grönberg, C. J. Zevenhoven, R. J. Ilmoniemi, and J. Hassel, "All-planar SQUIDs and pickup coils for combined MEG and MRI," *Superconductor Science and Technology*, vol. 24, no. 7, p. 075020, 2011.

[14] K. C. J. Zevenhoven, S. Busch, M. Hatridge, F. Öisjöen, R. J. Ilmoniemi, and J. Clarke, "Conductive shield for ultra-low-field magnetic resonance imaging: Theory and measurements of eddy currents," *Journal of Applied Physics*, vol. 115, no. 10, p. 103902, 2014.

[15] M. Hämäläinen, R. Hari, R. J. Ilmoniemi, J. Knuutila, and O. V. Lounasmaa, "Magnetoencephalography—theory, instrumentation, and applications to noninvasive studies of the working human brain," *Reviews of Modern Physics*, vol. 65, no. 2, pp. 413–497, 1993.

[16] J. O. Nieminen, P. T. Vesanen, K. C. J. Zevenhoven, J. Dabek, J. Hassel, J. Luomahaara, J. S. Penttilä, and R. J. Ilmoniemi, "Avoiding eddy-current problems in ultra-low-field MRI with self-shielded polarizing coils," *Journal of Magnetic Resonance*, vol. 212, no. 1, pp. 154–160, 2011.

[17] K. C. Zevenhoven, H. Dong, R. J. Ilmoniemi, and J. Clarke, "Dynamical cancellation of pulse-induced transients in a metallic shielded room for ultra-low-field magnetic resonance imaging," *Applied Physics Letters*, vol. 106, no. 3, p. 034101, 2015.

[18] W. R. Myers, *Potential Applications of Microtesla Magnetic Resonance Imaging Detected Using a Superconducting Quantum Interference Device*. Doctoral dissertation, University of California, Berkeley, 2006.

[19] T. P. Orlando and K. A. Delin, *Foundations of Applied Superconductivity*. Addison-Wesley Publishing Company, 1991.

[20] J. Charles P. Poole, H. A. Farach, R. J. Creswick, and R. Prozorov, *Superconductivity*. London: Academic Press, second ed., 2007.

[21] Y. Iwasa, *Case Studies in Superconducting Magnets: Design and Operational Issues*. Springer US, second ed., 2009.

[22] M. N. Wilson, *Superconducting Magnets*. New York: Oxford University Press, 1983.

[23] A. A. Abrikosov, "On the magnetic properties of superconductors of the second group," *Soviet Physics Jetp*, vol. 5, no. 6, pp. 1174–1182, 1957.

[24] V. R. Karasik and I. Y. Shebalin, "Superconducting properties of pure niobium," *Soviet Physics JETP*, vol. 30, no. 6, pp. 1068–1075, 1970.

[25] D. K. Finnemore, T. F. Stromberg, and C. A. Swenson, "Superconducting properties of high-purity niobium," *Physical Review*, vol. 149, no. 1, pp. 231–243, 1966.

[26] C. P. Bean and J. D. Livingston, "Surface barrier in type-II superconductors," *Physical Review Letters*, vol. 12, no. 1, pp. 14–16, 1964.

[27] E. Zeldov, A. Larkin, V. Geshkenbein, M. Konczykowski, D. Majer, B. Khaykovich, V. Vinokur, and H. Shtrikman, "Geometrical barriers in high-temperature superconductors," *Physical Review Letters*, vol. 73, no. 10, pp. 1428–1431, 1994.

[28] C. P. Bean, "Magnetization of hard superconductors," *Physical Review Letters*, vol. 8, no. 6, pp. 250–253, 1962.

[29] C. P. Bean, "Magnetization of high-field superconductors," *Reviews of Modern Physics*, vol. 36, no. 1, pp. 31–39, 1964.

[30] A. Ghosh, K. Robins, and W. Sampson, "Magnetization measurements on multifilamentary Nb3Sn and NbTi conductors," *IEEE Transactions on Magnetics*, vol. 21, no. 2, pp. 328–331, 1985.

[31] M. Ashkin, "Flux distribution and hysteresis loss in a round superconducting wire for the complete range of flux penetration," *Journal of Applied Physics*, vol. 50, no. 11, pp. 7060–7066, 1979.

[32] Y. Kato, M. Hanawaka, and K. Yamafuji, "Flux penetration into a wire of a nonideal type II superconductor in a transverse magnetic field," *Japanese Journal of Applied Physics*, vol. 15, no. 4, pp. 695–702, 1976.

[33] A. K. Ghosh, W. B. Sampson, E. Gregory, and T. S. Kreilick, "Anomalous low field magnetization in fine filament NbTi conductors," *IEEE Transactions on Magnetics*, vol. 23, no. 2, pp. 1724–1727, 1987.

[34] A. K. Ghosh, W. B. Sampson, E. Gregory, S. Kreilick, and J. Wong, "The effect of magnetic impurities and barriers on the magnetization and critical current of fine filament NbTi composites," *IEEE Transactions on Magnetics*, vol. 24, no. 2, pp. 1145–1148, 1988.

[35] K. Matsumoto, S. Akita, Y. Tanaka, and O. Tsukamoto, "Proximity coupling effect in NbTi fine-multifilamentary superconducting composites," *Applied Physics Letters*, vol. 57, no. 8, pp. 816–818, 1990.

[36] W. J. Carr, "Longitudinal field losses in multifilament superconductors over a range of frequencies," *Journal of Applied Physics*, vol. 48, no. 5, pp. 2022–2025, 1977.

[37] R. Körber, J.-h. Storm, H. Seton, J. P. Mäkelä, R. Paetau, L. Parkkonen, C. Pfeiffer, B. Riaz, J. F. Schneiderman, H. Dong, S.-m. Hwang, L. You, B. Inglis, J. Clarke, M. A. Espy, R. J. Ilmoniemi, P. E. Magnelind, A. N. Matlashov, J. O. Nieminen, P. L. Volegov, K. C. J. Zevenhoven, N. Höfner, M. Burghoff, K. Enpuku, S. Y. Yang, J.-J. Chieh, J. Knuutila, P. Laine, and J. Nenonen, "SQUIDs in biomagnetism: a roadmap towards improved healthcare," *Superconductor Science and Technology*, vol. 29, no. 11, p. 113001, 2016.

[38] J. D. Jackson, *Classical Electrodynamics*. John Wiley & Sons, third ed., 1999.

[39] E. Rosa and F. Grover, "Formulas and tables for the calculation of mutual and self-inductance (Revised)," *Bulletin of the Bureau of Standards*, vol. 8, 1912.

[40] Y. C. Hsu, P. T. Vesanen, J. O. Nieminen, K. C. J. Zevenhoven, J. Dabek, L. Parkkonen, I. L. Chern, R. J. Ilmoniemi, and F. H. Lin, "Efficient concomitant and remanence field artifact reduction in ultra-low-field MRI using a frequency-space formulation," *Magnetic Resonance in Medicine*, vol. 71, no. 3, pp. 955–965, 2014.

[41] M. Green, "Residual fields in superconducting magnets," in *Proceedings of the Fourth International Conference on Magnet Technology at Brookhaven National Laboratory*, pp. 339–346, 1972.

[42] M. Green, "Control of the fields due to superconductor magnetization in the SSC magnets," *IEEE Transactions on Magnetics*, vol. 23, no. 2, pp. 506–509, 1987.

[43] A. N. Matlashov, V. K. Semenov, and W. H. Anderson, "SQUIDs de-fluxing using a decaying AC magnetic field," *IEEE ESAS Superconductivity News Forum*, 2016.

[44] A. N. Matlashov, V. K. Semenov, and W. H. Anderson, "AC Defluxing of SQUIDs," *IEEE Transactions on Applied Superconductivity*, vol. 27, no. 4, pp. 12–16, 2017.

[45] S. M. Hwang, K. Kim, K. Kyu Yu, S. J. Lee, J. Hyun Shim, R. Körber, and M. Burghoff, "Type-I superconductor pick-up coil in superconducting quantum interference device-based ultra-low field nuclear magnetic resonance," *Applied Physics Letters*, vol. 104, no. 6, 2014.

[46] K. C. J. Zevenhoven, *Solving transient problems in ultra-low-field MRI*. Master's thesis, Aalto University and University of California, Berkeley, 2011.

[47] K. C. J. Zevenhoven, J. O. Nieminen, J. Dabek, P. T. Vesanen, L. T. Parkkonen, J. Simola, A. I. Ahonen, and R. J. Ilmoniemi, "Towards high-quality ultra-low-field MRI with a superconducting polarizing coil," in *11th European Conference on Applied Superconductivity (EUCAS 2013), Abstract 3A-EL-O4*, vol. 18, 2013.

A

Here, the integral in Eq. (50) for calculating the magnetic scalar potential of a magnetized loop is calculated using Wolfram Mathematica.

```
FullSimplify[Integrate[(Mz * z - Mρ * a + Mρ * ρ * Cos[ϕ]) /
    (z^2 + ρ^2 + a^2 - 2 * ρ * a * Cos[ϕ])^(3 / 2), {ϕ, 0, 2 * Pi}], Assumptions →
  {a > 0, Mρ ∈ Reals, Mz ∈ Reals, z ∈ Reals, ρ > 0, ρ^2 + a^2 + z^2 > 2 * ρ * a}]
```

$$
\frac{1}{a\left(z^2+(a+\rho)^2\right)^{3/2}}\left(\sqrt{1+\frac{4a\rho}{z^2+(a-\rho)^2}}\left(-a^2 M\rho+2aMz\,z+M\rho\left(z^2+\rho^2\right)\right)\text{EllipticE}\left[-\frac{4a\rho}{z^2+(a-\rho)^2}\right]-\right.
$$

$$
\frac{1}{\left(z^2+(a-\rho)^2\right)^{3/2}}\left(z^2+(a+\rho)^2\right)\left(\sqrt{z^2+(a-\rho)^2}\left(a^2M\rho-2aMz\,z-M\rho\left(z^2+\rho^2\right)\right)\text{EllipticE}\left[\frac{4a\rho}{z^2+(a+\rho)^2}\right]+\right.
$$

$$
M\rho\left(z^2+(a-\rho)^2\right)\left(\sqrt{z^2+(a+\rho)^2}\,\text{EllipticK}\left[-\frac{4a\rho}{z^2+(a-\rho)^2}\right]+\right.
$$

$$
\left.\left.\left.\sqrt{z^2+(a-\rho)^2}\,\text{EllipticK}\left[\frac{4a\rho}{z^2+(a+\rho)^2}\right]\right)\right)\right)
$$